REPORT ON THE FIRST CRYOGENIC PHOTON STOP EXPERIMENT

P. Bauer[1], R. Bossert, C. Darve, D. Erickson, K. Ewald,
M. Geynisman, A. Klebaner, P. Limon, A. Martinez, L. Pei

Fermilab

As part of Fermilab's recent Very Large Hadron Collider (VLHC) feasibility study, a water-cooled photon stop was proposed as a possible device to intercept the intense synchrotron radiation in the high field magnets with minimal plug-power. The photon stop, if feasible, promises not only significant savings in cooling power compared to a solution in which the synchrotron radiation is extracted from a beam screen at cryogenic temperatures, but also virtually removes the synchrotron radiation limitation to beam energy and luminosity in a future VLHC. Among the technological challenges regarding photon stops is their cryo-design. The photon stop is water-cooled and operates in a cryogenic environment. A careful cryo-design is therefore essential to enable operation at minimum heat transfer between the room temperature sections and the cryogenic parts. A photon stop cryo-design was developed and tested with success. The design of the first photon stop prototype has been presented elsewhere. This note presents the results of the first cryogenic photon stop experiment.

[1] email: pbauer@fnal.gov

TABLE OF CONTENT

1) INTRODUCTION

The next generation of large hadron colliders, following Cern's LHC, such as for example the proposed Very Large Hadron Collider, or VLHC [1], will be limited in energy reach and luminosity by the considerable synchrotron radiation power emitted by the beams when steered through the high field magnets. The synchrotron radiation power radiated by the VLHC in its high field magnet stage as proposed in [1], is 5 W/m per beam. This represents a ~50 fold increase of radiation power per unit length from the LHC level. It would be too costly to absorb this radiation at the low temperature of the cryogenic magnets. It is therefore necessary to develop solutions for a cost effective removal of the synchrotron radiation power. One such solution, discussed further in [1,2], is to insert a beam-screen into the magnet bore operating at an elevated temperature (of ~100 K) to absorb the heat load at an acceptable Carnot efficiency. In theory the best case would be to absorb the synchrotron radiation at room temperature. Water-cooled photon stops that protrude into the beam tube at the end of each bending magnet and scrape off the synchrotron light beam would represent such a solution. We have proposed such photon stops for future hadron colliders [3,4]. There are, however, some issues that need to be resolved as part of a proof of feasibility. Among them are geometrical issues related to magnet length and beam trajectory curvature as well as issues related to reflectivity (e.g. X-ray luminescence) as well as beam impedance. Some of these issues have been discussed in e.g. [3,4,5]. This document discusses an experiment that addresses another technological challenge of the photon stop - the cryo-design. The photon stop is water-cooled and operates in a cryogenic environment. A careful cryo-design is therefore essential to enable operation at minimum heat transfer between the room temperature radiation absorber and the parts at cryogenic temperatures. A photon stop cryo-design was developed, (see [5] for s description of the design) and a first photon stop prototype was built (the drawings are available under the Technical Division ER# 7223). The photon stop prototype was assembled into an experimental mock-up of a magnet interconnect, including a short section of beam screen and submitted to a test. This note presents the results of the first successful cryogenic photon stop experiment.

The first photon stop prototype is shown in Figure 1. It consists of the water-cooled copper tube, that is the radiation absorber, surrounded by an inner and an outer shield. The shielded absorber is assembled into a mock-up of the magnet inter-connect consisting of a short (~1 m) section of cold mass and beam screen. As clearly shown in Figure 1 the absorber enters perpendicularly into the cold-bore / beam-screen assembly such as in a real accelerator environment. The inner photon stop thermal shield is cooled with a cooling spiral to ~80 K throughout the bottom half and negotiates a temperature drop from room temperature to ~80 K through bellows forming its upper half. The lower, 80 K part of the inner shield in turn is surrounded by an outer shield, which, also through bellows, negotiates a temperature drop from ~80 K at its top to ~5 K at the bottom, where it is welded to the cold bore. In Figure 1 only the outer shield bellows are visible and the lower part of the inner shield is therefore not visible. The cold bore is in fact a 60" long, 3"∅ copper tube cooled with a spiral containing liquid helium at ~5 K. It
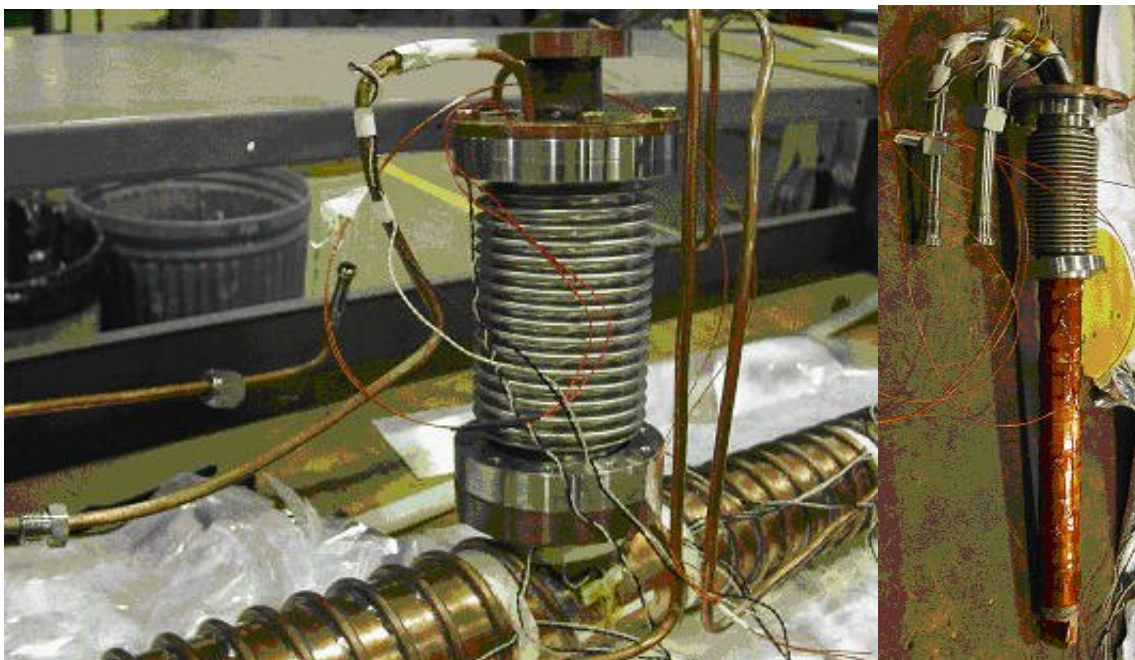
Figure 1: Photon stop prototype for the first cryogenic design experiment. Left: cold bore mock-up (horizontal) with photon stop shield assembly (vertical). The inner shield is within the outer shield bellows. The tubes supplying the inner shield with ~80 K gaseous He (GHe) can be seen. Right: absorber with inner shield top bellows. The water pipes are clearly visible. The absorber is instrumented with safety heaters.

also contains a dummy beam screen running along its entire length as a shield from the radiation emitted by the photon-stop tip. The beam screen is cooled to ~80 K with helium gas. The complete photon-stop cryo-assembly was mounted into a vacuum vessel (with its own ~80 K radiation shield) and supplied with water as well as liquid helium and 50-100 K helium gas from a liquefier. Instrumentation was installed on the various circuits to measure cryogen flow and temperature profiles. The synchrotron radiation heating was simulated with heaters mounted on the photon stop tip. Heaters were also mounted on the cryogenic circuits to measure the thermal interference between the different temperature stages using the so-called heater technique. The following will discuss the setup of the cryo-experiment (chapter 2), the results of the experiments (chapter 3) and the results of the data analysis (chapter 4). Additional illustrations of the photon stop test setup, can be found in appendix A. The appendices also contain a discussion of the heater characteristics (B), the flowmeter calibration measurements (C), an analysis of the temperature measurement error for the Platinum and Cernox temperature gauges (D), the safety review report (E), a purchase summary (F), the mcad spreadsheet with the model calculations (G), the experimental raw data (H), and the temperature sensor calibrations (I).

2) PHOTONSTOP CRYOTEST SETUP

2.1) Photon Stop Assembly

The photon stop assembly has been described in detail in [5]. Figure 2 shows the main components of the photon stop absorber assembly. The absorber (on the left in Figure 2) consists of a 1.25" $\varnothing$, 19.75" long copper tube with a nose-piece (the actual absorber) welded to it at one end and a flange welded to it on the other end. The flange allows mounting of the absorber to the inner shield. The flange has two holes for the passage of two 0.5" $\varnothing$ stainless steel water tubes (0.03" wall thickness). At the seam between the photon stop nose-piece and the copper tube are three G10 pins (5 mm $\varnothing$, 5 mm long) distributed around the tube perimeter. The photon stop is in direct (conductive) thermal contact with the inner shield only through the G10 centering pins
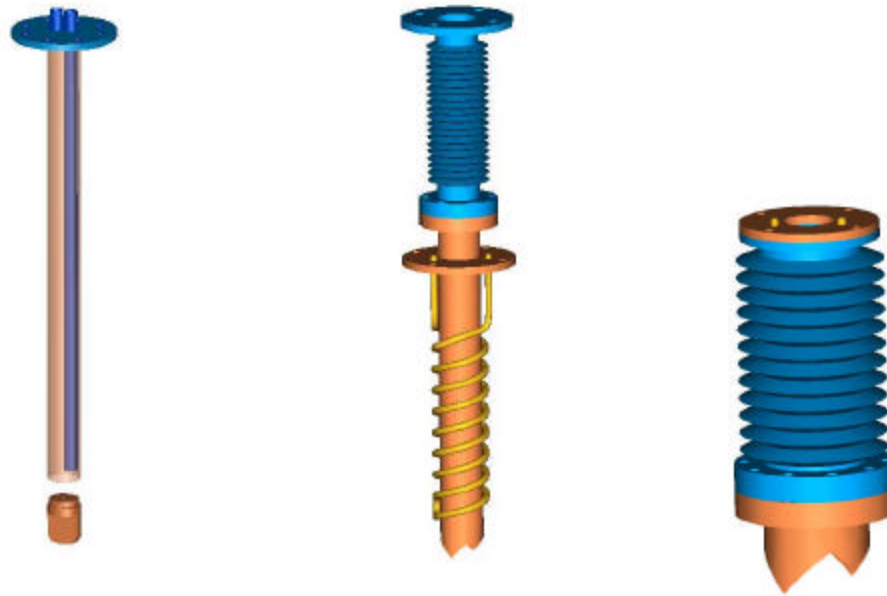

Figure 2: Exploded view of photon stop: absorber (left), inner shield (middle) and outer shield (right). Blue indicates steel, orange indicates Copper.

and through the top flange. The brazing between the copper tube and the nose-piece would not be permissible in the accelerator, because of the potential risk of beam vacuum contamination. In fact, the absorber had to be replaced in the course of this test after a leaking helium valve led to an unexpected cool-down of the system, freezing water that had been left stagnant in the absorber (Figure 3 shows the damaged photon stop after the incident).

The photon stop thermal shield (so called inner shield, shown in the middle in Figure 2) has to negotiate a temperature drop from ambient at its top to ~80 K (or less) at the mid-section and below and absorb the thermal radiation from the 300-400 K insert in its core. It consists of a 1.5" $\varnothing$ copper tube (wall thickness=0.03") with a brazed cooling spiral (0.75" pitch, 0.25" tube $\varnothing$, 0.03" wall thickness) on the lower part and a 7.25" long stainless steel bellows (24" thermal length, 0.006" thickness) as the top part, connected by a mixed steel/copper flange. At the bottom the inner shield is welded to the beam screen. At the top end the shield is at room temperature and bolted to the top flange of the water-cooled photon stop.
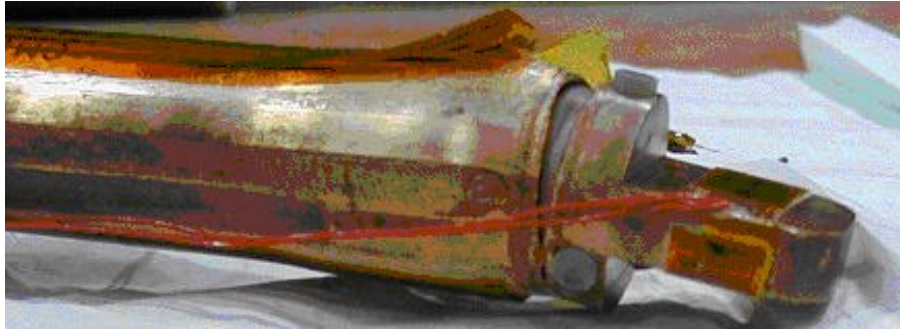
Figure 3: Freezing of stagnant water caused the photon stop to burst. Also shown are the heaters that simulate the synchrotron radiation heating and the G10 centering pins.

Figure 4: Cold-bore assembly for the photon stop cryo-test. Upper left: beam-screen and cold-bore center before insertion of photon stop. Lower left: G10 spider separating beam screen and cold bore. Right: beam screen cooling tube and cold bore cooling spiral.

The outer thermal shield (right in Figure 2) is composed of a 3"⌀ copper saddle and flange, stainless steel flanges and a 3"⌀, 7.25" long stainless steel bellows (25.4" thermal length, 0.006" wall thickness). On top it is bolted to a copper flange, which is welded to the inner shield mid-section. At the bottom the outer shield is welded to the cold bore. The outer shield stainless steel bellows negotiate the temperature drop from ~80 K at the top to the cold-bore temperature (~5 K) at the bottom.
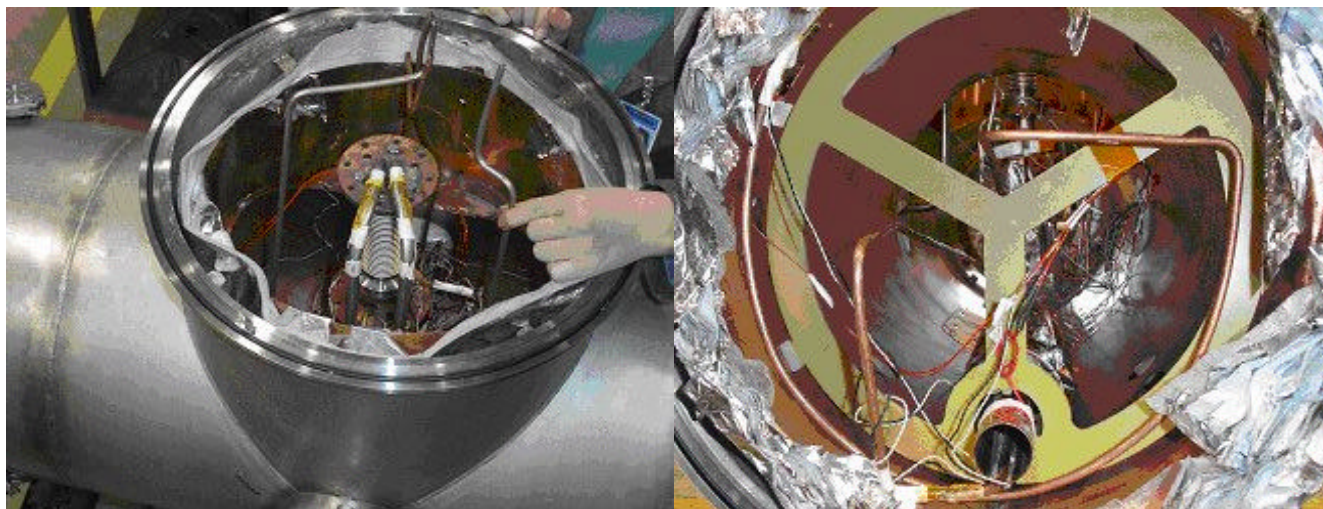
Figure 5: Photon stop assembly in cryostat. Left: top-view, Right: side-view.
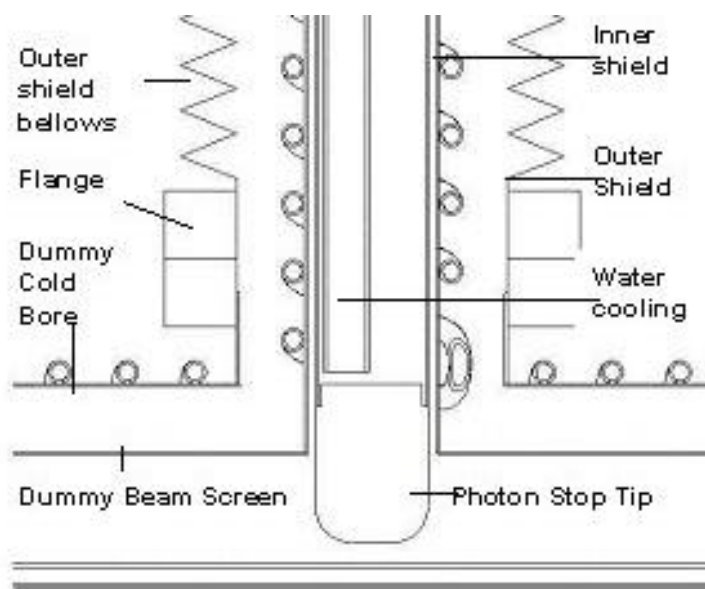
Figure 6: Cross-section through photon stop cryo-test assembly, detail.

Figure 4 shows different views of the cold bore – beam screen assembly. The 60" long dummy beam screen tube (1.5" $\varnothing$) is inserted into the similarly long dummy cold-bore tube (3" $\varnothing$), supported with G10 spiders at both extremities (Figure 4). The cold-bore tube is cooled to ~5 K from the outside by a 0.75" pitch, 0.25" $\varnothing$ cooling tube spiral with liquid helium (LHe) flow. The wall thickness of the cold-bore tube is 0.125". The beam screen is maintained at ~80 K temperature with a copper cooling tube welded to it along its length. Both, the cold bore and the beam screen tubes are made of copper to facilitate the cooling. The spider (0.1875" thickness, three contact pins of width 0.125")

is a critical part of the cryo-design because it is the only mechanical connection between the 80 K beam screen and the 5 K cold-bore.

The photon stop assembly was installed into a cryostat, shown in Figure 5, using large G-10 spiders (0.25" thickness, ~ 1m diameter, 1 inch width, shape: Y in circle). The beam screen is supported by the G10 spiders in three points at each end, such that the total thermal contact area between the beam screen and cryostat thermal shield is approximately 1"×0.25".   The helium transfer lines enter the cryostat through the top access window.   The water lines enter through the small side-ports in the middle of the cryostat.

Figure 6 shows a schematic of the region close to the absorber nose-piece. As can be seen clearly in this picture the room-temperature insert is surrounded everywhere by an intermediate temperature shield, such as to prevent any direct conductive or radiation contact with the 5 K cold-bore.

2.2) Interface to Refrigerator

The experimental setup was incorporated into the cryogenic system of Fermilab's Meson cryogenics lab. The Meson lab refrigerator supplied 5 K and [30-80] K helium to the photon stop assembly and recovered the helium at ambient temperature.   The refrigerator is of CTI design with STAR-type heat exchangers, liquid nitrogen pre-cool and CTI reciprocating expansion engines. The refrigerator was coupled with a 4,000 liter helium dewar for the production output and regeneration of boil-off, and with a 225 m^3 warm helium storage buffer.   The refrigerator and the experimental setup were operated and monitored with a Siemens Advanced Process Automation and Controls System (APACS). The refrigerator has a design capacity of 600 watts at 4.5 K or ~4 g/s of liquid helium, but was found to be limited to ~1 g/s of 5 K plus 1 g/s 30 K at mixed mode of operation.   That necessitated running the experiment in a batch mode when helium flows to the experiment were higher than 1 g/s.

5 K two-phase helium was drawn from the exhaust of the "wet" expansion engine (WE).   30 K helium was drawn from the inlet of the "dry" expansion engine (DE).   A transitional valve box (BR), vacuum insulated U-tubes and hoses, and a transitional vertical vacuum vessel were used to route the helium flow from the refrigerator to the photon stop cryostat.   Figure 7 shows the experimental setup, including the distribution box and the cryostat containing the photon stop.   The photon stop experiment schematic in Figure 8 also shows some details of the cryogenic circuits.

The "BR" valve box was used exclusively as a transition element to route cold helium flows from the refrigerator to the experiment. It provided connections for an in-line control valve (EVWHS) and a 800 W heater (HTR1) to control mass flow and temperature of 30 K helium to the photon stop experiment.   The helium flows from the "BR" valve box were routed to a vertical vacuum vessel via standard vacuum jacketed U-tubes.   The purpose of the vertical vessel was to be a portal to and from the cryostat, which housed the photon stop experimental setup.   The vertical vessel had a 4" OD connection to a simplified transfer line, through which helium was routed to and from the photon stop cryostat via ¼" tubing.   The tubing inside the vacuum transfer line was thermo insulated and supported with common G10 spiders.   Helium pressures were

measured in the supply and return lines thus allowing for properties calculations. The pressures of the cold and warm helium were measured with either Setra™ or Stellar™ transducers. The temperature measurements, though, were taken only in the photon stop cryostat.

The return lines were taken outside the vertical vacuum vessel for warming helium with electric heaters (HTR2 and HTR3) and returning it to the refrigerator suction. The warm-up tubing was from 3/4" to 1" diameter and contributed less then 1 psi of pressure drop. The temperature-controlled electric heaters HTR2 (15 kW) and HTR3 (1 kW) were installed in the 30 K and 5 K lines in order to warm up helium upstream of the flowmeters.

The flow of the 5 K helium was measured at the warm end by using an Omega™ turbine flowmeter model SP0717 attached to FTB-937 turbine housing of 29.65 mm ID. The flow of the cold helium gas for the shields was measured with Aeroquip Barco™ 1-1/4"- 588 Venturi flowmeter. The calculations for the helium mass flows were adjusted for flowing temperature and pressure to compensate for density variations. The volumetric water flow was measured with Aeroquip Barco™ 1"- 567 Venturi flowmeter. Appendix C contains a detailed discussion of the flowmeter calibration measurements. The mass flow of 5 K helium was controlled with a modified Cryolab™ valve EVCHR ($Cv = 2$) installed in the warm end of the flow path. The mass flow of the 30 K helium was controlled with a modified Cryolab™ valve EVWHS ($Cv = 0.32$) installed in the cold inlet of the flow path.

The refrigerator/photon stop interface was adapted from existing equipment with a minimum of modifications. Unfortunately it did not allow the transfer of liquid helium from the refrigerator to the photon stop cold bore. An estimated 11 W of parasitic heat load was warming up the 5 K helium to ~11 K (in the best case). We believe that one third of the heat load entered via the 2 bayonet connections in the valve box (~1.4 W/bayonet), and the rest through the G10 supports in the 2 m long transfer line. An unsuccessful attempt was made to cool a section of the transfer line with liquid nitrogen (see frozen transfer line vacuum jacket in Figure 7, right plot). Furthermore, the cold-bore cooling spiral, made from 0.25" cooling tube, proved to have an insufficient diameter to allow for large enough mass-flow in the case of the 10 K GHe (it was designed for liquid). Only a maximum of 1.5 g/s of flow could be achieved, therefore further restricting the reach toward low temperature. Given this limitation, the decision was taken, to operate the cold bore at several temperatures between 10-20 K and to extrapolate the results toward 5 K.

The 30-80 K circuit, on the other hand, could be successfully operated (once a burned out heater was replaced). The feedback loops regulating the gas temperature and the flow worked well and allowed to run several experiments with shield temperatures varying between 40 and 80 K. The flow variations remained within ~5 %. A safety review was conducted. The safety report is given in appendix E.
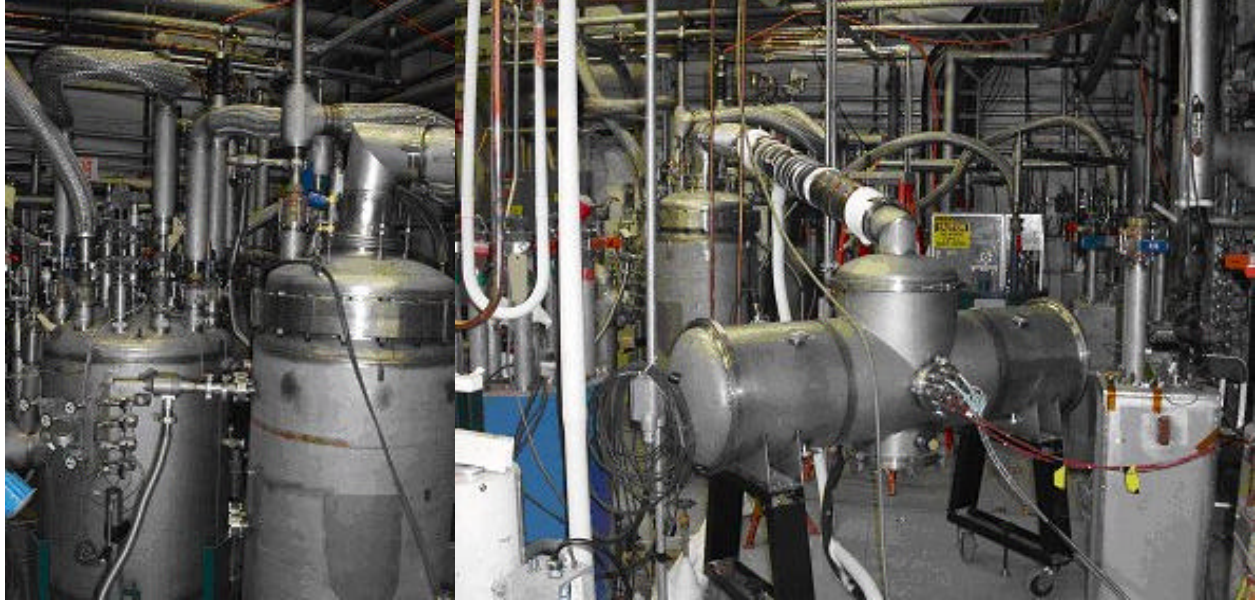
Figure 7: Left: Valve box for helium circuits. Right: cryostat with photon stop.

2.3) Instrumentation and Controls

Table 1 lists the entire instrumentation for the photon stop cryo-test. The list includes temperature sensors, heaters and flow-meters. It also defines the variable names given to the different sensors in ACNET and specifies the ranges and types of signals produced. Figure 8 shows a schematic of the photon stop experiment circuitry and instrumentation. Figure 9 shows a snapshot of the ACNET interface that continuously reported (every 30 sec) the acquired data. The following discusses the instrumentation of the three major sub-systems of the photon-stop assembly: 1) the shield circuit, comprising the photon stop inner shield, the cryostat shield and the beam screen cooled in series with GHe at ~50 K; 2) the 5 K LHe circuit cooling the cold mass; and 3) the water circuit.

As described above, the shield circuit was supplied with 50 K helium gas from an intermediate temperature stage in the refrigerator at controlled rates varied from 1 to 5 g/s. The gas was then warmed up with a 700 W heater to a set-temperature. The heater power was controlled with feedback from a down-stream temperature sensor (PT102 sensor TPPTSI). The flow was regulated with an automatic valve (VWHS) in a feedback circuit with a Venturi flowmeter (FTCO) at the down-stream end of the circuit. In addition the pressure was read in an upstream sensor (PTCOIN). Finally, before being returned to the refrigerator the gas was heated up to ambient temperature (with a 15 kW heater). Six Platinum (Pt) temperature sensors (PT102 type) were distributed along this circuit: at the entrance (TPPTSI) and exit (TPPTSO) of the photon stop inner shield, the cryostat thermal shield (TPTSIN, TPTSOU) and the beam screen (TPBSIN, TPBSOU). The calibration and estimated measurement error of the Pt temperature sensors is discussed in appendix C. The input and output pressure in the GHe circuit was also measured (PTCOIN, PTCOOU) to determine the pressure drop. Each of these circuits was also equipped with an electrical heater in order to allow application of heat loads in the range 10-50 W, to measure the residual heat load on each of the components with the

so-called heater-technique. These heaters are labeled YPTS (photon stop inner thermal shield), YTS (cryostat thermal shield), YBS (beam screen). The heater characteristics are discussed in detail in appendix B.

The 5 K circuit, which as explained above, was actually operated with ~10-20 K GHe, was equipped with LakeShore™ Cernox temperature sensors, heaters and flow meter (and flow regulation). The temperature of the incoming gas was varied by changing the flow within the range of 0.3 to 1.2 g/sec. The flow was controlled with a
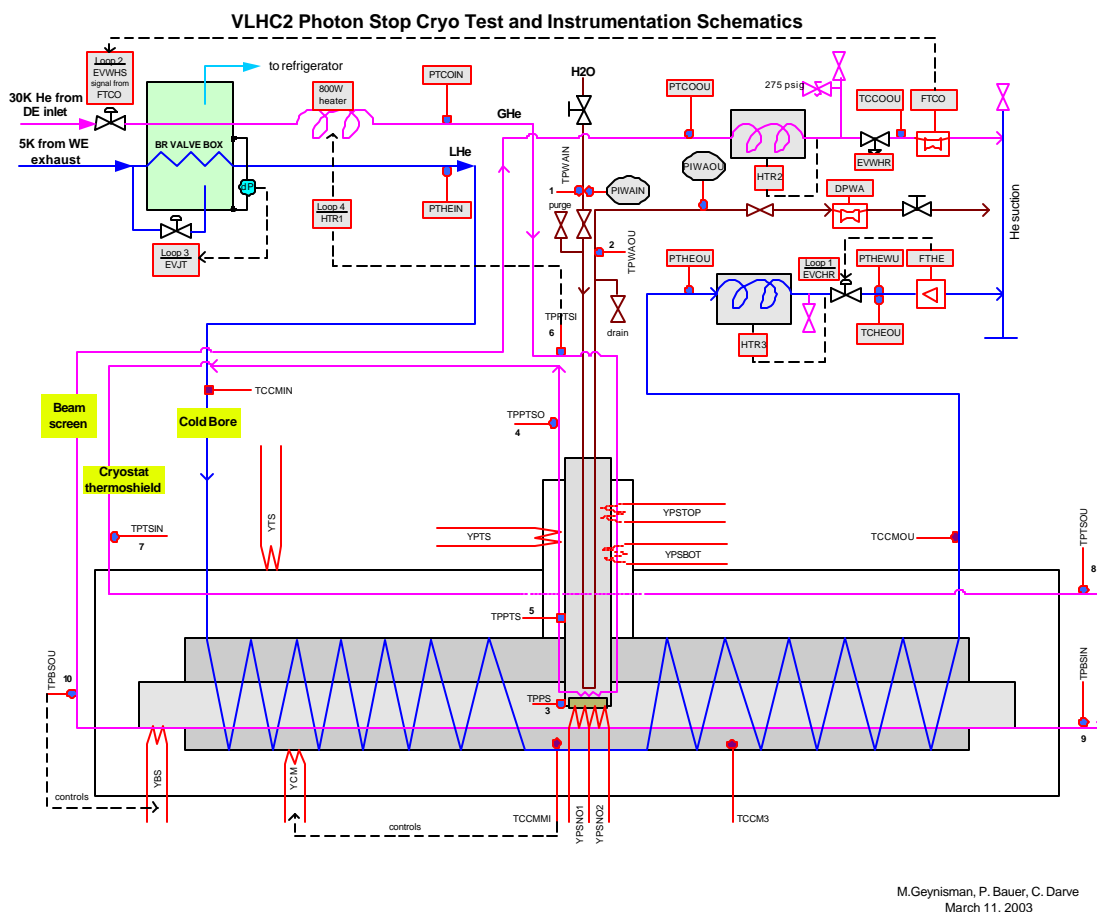
Figure 8: Flow schematic for the photon stop test.

feedback loop by an automatic valve EVCHR based on the signal from the FTHE flowmeter (Omega, see calibration in appendix C). The four Cernox temperature sensors were distributed along the cold bore tube: number one (TCCMIN) was attached to the cooling tube at the beginning of the cold bore cooling spiral, number two was attached to the cold bore tube in the middle section (TCCMMI), number three was attached to the cold bore at ~3/4 of the way and finally the last sensor (TCCMOU) was mounted on the cooling tube exiting the cold bore spiral. The calibration and the estimated measurement errors of the four Cernox sensors are discussed in appendix D. A 50 W heater (YCM) was also mounted on the cold-bore tube, close to the sensor TCMMOU at the

downstream end. This particular heater, as will be discussed in further detail in the context of the data-analysis, was placed at the downstream end of the 5 K circuit (instead of at the upstream end, as planned). Therefore, so it is believed, the heater also affected the TCMMOU temperature sensor via direct conduction, thus slightly modifying the results of the measurements based on the heater method. This issue will be discussed in further detail in the context of the data analysis. The input and output pressure in the LHe circuit was also measured (PTHEIN, PTHEOU) to determine the pressure drop. After exiting the photon stop assembly the cryogen was warmed up to ambient with a 1 kW heater. This was also necessary because the flow-meter is calibrated for ambient gas only.

The water circuit was equipped with a flow-meter (the flow regulation was manual), and two Pt temperature sensors (TPWAIN, TPWAOU) as well as pressure sensors (PIWAIN, PIWAOU), mounted on the stainless steel cooling tubes, to measure the temperature and pressure of the in and out-coming water. The synchrotron radiation heating was simulated with two heaters (YPSNO1, YPSNO2) mounted on the photon stop tip, together with a Pt temperature sensor (TPPS) to measure the tip temperature. A set of safety heaters (YPSTOP, YPSBOT) was also mounted on the photon stop in order to prevent accidental freezing. Following the bursting of the photon stop, safety measures were enforced, such as an automatic closure of all helium valves in the case of loss of water flow or the safety heaters, and additional safety measures provided, such as a manual compressed air line to blow out water from the stop. This feature proved to very useful in the course of the experiment as it turned out that the only way to increase the photon stop tip temperature noticeably was to remove the water from the PS.

The Cernox and Platinum temperature sensors were mounted to the photon stop with VGE1731 varnish. This operation had to be repeated once because the temperature sensors were not well attached the first time. Heaters are made of Nickel-Steel alloy foil encapsulated in Kapton™ foil. The alloy is such that the resistance change at low temperature is very small (<1%, see appendix B). They were affixed with STYCAST™ to the different parts of the photon stop and supplied with current through manganese wires to reduce thermal conduction into the cryostat. All instrumentation wires were routed to the lateral exit ports of the cryostat and transited through the vacuum barrier via several Burndy™ connectors mounted into the flanges.

The data acquisition system in Meson is built on the industrial Siemens-Moor APACS automation system. At the same time, the data should go to the ACNET system, which is a Fermilab site-wide standard. ACNET allows for integration of data into Fermilab control system, including an ability of powerful data logging and site-wide access. ACNET is an UDP/IP based low-level Internet protocol. From the client side it is supported by a VAX based system – a set of applications and services written in C using proprietary CLIB and by "new" Java-based Data Acquisition Engines. A set of new Java applications, almost as functional as VAX, exists to read data from Data Acquisition Engines and present this data to users.

The APACS control system, as briefly described below, allowed reading out the above listed instrumentation and relaying the information to the ACNET system with its dataloggers for storing and displaying the data. The Siemens APACS 32 Bit Application

Table 1: Photon stop cryo-test instrumentation list.

Tag	ACNET	Function	Type	Manuf-r	Raw data	Range	Measured at 300 K
TCCMIN	TC01	T:cold mass in	CX-1050-SD	L.Shore	0-10VDC	4-330K	128.19Ohm
TCCMMI	TC02	T:cold mass middle	CX-1050-SD	L.Shore	0-10VDC	4-330K	128.99Ohm
TCCM3	TC03	T:cold mass 3/4	CX-1050-SD	L.Shore	0-10VDC	4-330K	128.98Ohm
TCCMOU	TC04	T:cold mass out	CX-1050-SD	L.Shore	0-10VDC	4-330K	128.92Ohm
TPWAIN	TP01	T:water in	PT102	L.Shore	0-5VDC	14-873K	172.05Ohm
TPWAOU	TP02	T:water out	PT102	L.Shore	0-5VDC	14-873K	173.48Ohm
TPPS	TP03	T:photon stop nozzle	PT102	L.Shore	0-5VDC	14-873K	169.90Ohm
TPPTSO	TP04	T:photon stop TS out	PT102	L.Shore	0-5VDC	14-873K	169.48Ohm
TPPTS	TP05	T:photon stop TS middle	PT102	L.Shore	0-5VDC	14-873K	169.70Ohm
TPPTSI	TP06	T:photon stop TS in (gas helium in)	PT102	L.Shore	0-5VDC	14-873K	168.81Ohm
TPTSIN	TP07	T:cryostat TS in	PT102	L.Shore	0-5VDC	14-873K	170.97Ohm
TPTSOU	TP08	T:cryostat TS out	PT102	L.Shore	0-5VDC	14-873K	170.80Ohm
TPBSIN	TP09	T:beam screen in	PT102	L.Shore	0-5VDC	14-873K	169.52Ohm
TPBSOU	TP10	T:beam screen out	PT102	L.Shore	0-5VDC	14-873K	168.20Ohm
YPSTOP	YP01	Y:photon stop top	Resistor	Omega	0-4VDC	0-50 W	15.50 Ohm
YPSBOT	YP02	Y:photon stop bottom	Resistor	Omega	0-4VDC	0-50 W	16.0 Ohm
YPSNO1	YP03	Y:photon stop nozzle (in series with YPSNO2)	Resistor	Minco	0-4VDC	0-50 W	5.40 Ohm
YPSNO2	YP04	Y:photon stop nozzle 2	Resistor	Minco	0-4VDC	0-50 W	5.30 Ohm
YPTS	YP05	Y:photon stop TS	Resistor	Omega	0-4VDC	0-50 W	15.49 Ohm
YTS	YP06	Y:cryostat TS	Resistor	Omega	0-4VDC	0-50 W	4.80 Ohm
YBS	YP07	Y:beam screen	Resistor	Omega	0-4VDC	0-50 W	15.37 Ohm
YCM	YP08	Y:cold mass	Resistor	Omega	0-4VDC	0-50 W	15.66 Ohm
PTHEIN	PT01	P:5K helium cold in	PT	Setra	0-5VDC	0-50 psia	N/A
PTHEOU	PT02	P:5K helium cold out	PT	Setra	0-5VDC	0-50 psia	N/A
PTHEWU	PT03	P:5K helium warm out	PT	Setra	0-5VDC	0-50 psia	N/A
PTCOIN	PT04	P:80K helium cold in	PT	Stellar	0-5VDC	0-250 psig	N/A
PTCOOU	PT05	P:80K helium warm out	PT	Stellar	0-5VDC	0-250 psig	N/A
TCHEOU	TT01	P:5K helium warm out	T-type TC	none	none	none	N/A
TCCOOU	TT02	P:80K helium warm out	T-type TC	none	none	none	N/A
FTHE	FT01	F:5K helium out	Turbine SPO1 1/4-CB-PH15-B-4RFX	Omega	0-5VDC	0-1000 Hz	
FTCO	FT02	F:80K helium out	Venturi	Barton	4-20 mA	0-30"H2O	
DPWA	FT03	F:water out	Venturi	Barton	4-20 mA	0-60"H2O	
HTR1	Y1I	Y:80K helium cold in	Resistor	N/A	N/A	0-700 W	

Programmer's Interface (API) Toolkit allowed production by BD/Controls staff of custom PC-based programs used to send and retrieve information from an APACS system. Communication between a second PC used for ACNET interface and the APACS system was by MODULBUS and a MODULBUS Interface card. APACS

variables were converted in the PC to values useable by BD/Controls standard PC resident Data Acquisition Engine (DAE) code and then passed on to the ACNET system.

APACS-based control system at Meson is interconnected to ACNET via the Data Acquisition Engines (DAE) prototyped by Access Clients (OAC). DAE call the OAC procedures for acquiring device reading and transport it to ACNET. Special OAC was written to read and set the devices on APACS. This OAC acts as a bridge. It reads the list of controlled devices during initialization of the database, sets up a list of APACS devices in the Siemens-Moor system and then reads the devices with a preset frequency of 2 Hz. The reading frequency is a variable parameter. This OAC expose values read from APACS to the ACNET system. It is written in Java, as everything in the DAE. To communicate with APACS a Java Native Interface (JNI) was used with an added library of C routines compiled in Cygwin. This library allows any Java program to read and set APACS devices. To simplify the bridge only double and integer readings and settings were used, so no status or control properties for these "APACS-ACNET" devices are possible. All logical information is presented as integer 0 or 1. Settings to APACS are processed as soon as they are received from the ACNET.

Figure 9 shows a snapshot of the ACNET interface designed for the photon stop test. The interface displays the instantaneous values (0.2 Hz) of all instrumentation parameters.
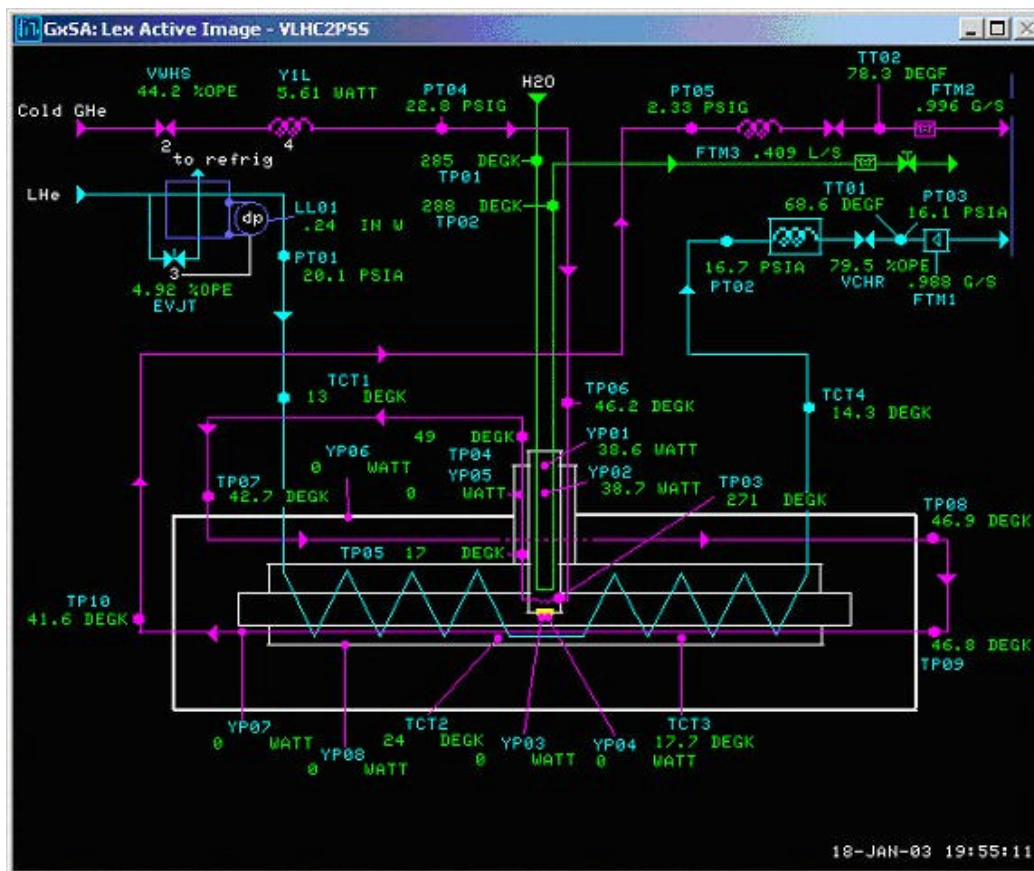

Figure 9: Snapshot of photon stop ACNET interface.

3) PHOTON STOP CRYOTEST PROCEDURE AND TEST RESULTS

3.1) Measurement Goals and Principle

The goals of the photon stop cryo-test were, a) to prove feasibility of the photon stop cryo design; and b) to quantify the residual heat load on the different components due to thermal cross talk in order to determine the efficiency of the photon stop technology.   In addition, the data were used to validate the model calculations presented in chapter 4.

The most important goal of the photon stop cryo-test was to prove that in its current design configuration the photon stop could operate over extended periods of time without major incidents. A long term goal of the development of photon stops for an accelerator environment would be to limit the heat load on the 4 K stages to less than ~1 W. The power limits regarding the 80 K temperature stages (e.g. photon stop thermal shield and beam screen) are less stringent given the strongly reduced Carnot penalty at these higher temperatures.

The measurement of the residual heat load on the various sub-systems of the photon stop assembly, such as (in order of importance) the cold bore, the photon stop inner shield, the beam screen and the cryostat thermal shield, was obtained on the basis of two methods.

–1- The first method consisted in measuring the temperature difference DT across each sub-system for each equilibrium configuration. Then the residual (or static) heat load, Q_0, was derived from equation (1),

$$Q_0 = \dot{m} C_p \left(T_{out} - T_{in} \right) \qquad , \tag{1}$$

where: $\dot{m}$ is the mass flow of helium cooling the sub-system (typically 1 g/sec), C_p the cryogen specific heat (~5.2 J/K/g in cold helium), and $(T_{out}-T_{in})$ the measured temperature difference over the cooling section containing the source of applied heat.

-2- Since the residual heat load was expected to be low for some configurations, a more precise method, the so-called heater-method was used. The heater method uses heaters attached to the circuit of interest to raise the temperature of the cryogen with a known amount of heat input. The temperature rise of the cryogen as a result of different applied heater powers can be used to extrapolate to the case of zero heater power, which is assumed to be that of the heating due to the residual heat load only. In order to be precise, the method requires a constant flow in the cryogen. The extrapolations derived with the heater method can also be compared to the static temperature distribution, which reflects the same residual heat-load (often the static measurements are less precise). The determining equation for the heater method measurement is given in (2), where Q_{el} is the applied electrical heater power, and Q_0, $\dot{m}$, C_p and $(T_{out}-T_{in})$ are as defined above.

$$Q_{el} + Q_0 = \dot{m} C_p \left(T_{out} - T_{in} \right) \tag{2}$$

The linearity of the relation between DT and Q_{el} allows extrapolation to $Q_{el}=0$, in which case the factor Q_0, the static heat load can be determined.

3.2) Test Procedure

Before start of the test the photon stop cryo test system was commissioned. Leak checking was performed on all circuits. The resistance of heaters and temperature sensors was measured and the automatic regulation loops tested. Then the refrigerator was started and several days later the cool-down of the photon stop system could start. As discussed above it was found that the LHe circuit could not be operated at 5 K because of excessive heat load in the transfer line. Therefore the 5 K circuit was operated at ~15 K instead. It was also found that the refrigerator could not produce more than 1 g/s of 5 K and 30 K helium at the same time. Therefore, when larger flow was required, the refrigerator was operated in a batch mode. Unfortunately, the combination of the available LHe dewar pressure (less than 1.7 atm) and the pressure drop in the supply line to the cryostat necessitated a flow less than ~1g/s in the 5 K circuit. The shield circuit, however, was operated with a flow of up to 5 g/s (in the batch mode). Once the stable flow and temperature conditions had been achieved, the measurements could start.

The standard procedure consisted in varying the heater power in three steps (typically 10, 25 and 50 W) and recording the temperature distribution in the entire system after thermal equilibrium had been achieved. This particular method of measurement is described above and referred to as the "heater-method" (or method 2). Thermal response times were typically of the order of minutes (20 minutes worst case). The conditions at zero heating power, before and after the heater test were recorded, therefore also providing information on the static heat load (method 1). That procedure was repeated for all circuits of interest, namely the photon stop thermal shield, the cryostat thermal shield, the beam screen, and the cold mass. The cold-mass measurements are considered to be the most important, given that it is the system with the lowest operating temperature. Various different cases were studied in which the following parameters were varied:

- operating temperatures in the shield circuit (45-77 K)
- operating temperature in the cold mass circuit (15-25 K)
- flow in the shield circuit (1-5 g/s)
- flow in the cold mass circuit (0.3 – 1.2g/s)
- temperature of the photon stop water cooling circuit (80 – 300 K)
- temperature of the photon stop nose (80 – 400 K)

To vary the temperature of the photon stop water circuit it was necessary to blow out the water from the photon stop and to cool with compressed air flow only. The low temperature operating point (80 K) was achieved using liquid nitrogen (LN) instead of water. During the course of an early test the cryostat thermal shield heater, *YTS*, was burned. Also, in later stages of the experiment, the photon stop nose heaters (*YPSNO1*, *YPSNO2*) were both burned. That, however, did not have dramatic consequences, since the safety heaters, *YPSTOP* and *YPSBOT*, could also be used to heat the photon stop

nose.   A log-book archive of all measurements can be found online at:
http://tdserver1.fnal.gov/nicol/lhc_irq_cryostat/ch_darve/photon_stop/PS.htm.

3.3) Example of Measurement

The following describes, in five steps, a measurement for a specific configuration (called case B, see configuration parameters in Table 2). The goal of the measurement is to determine the residual heat load in each of the four major sub-systems, i.e. the dummy cold mass, and the warm helium circuits (photon stop thermal shield, cryostat thermal shield and beam screen).   The description of the flow schematic and the location of temperature sensors are given in chapter 2.3).

Table 2: Temperatures and mass flow configuration for case B

	Average temperature (K)	Mass flow (g/s)
Cold helium	14.6	1.0
Warm helium	77.0	1.0
Water	271	-

As explained in chapter 3.1 the heat load is calculated from the heat balance equation (equations (1) and/or (2)).   In order to generalize the expression to the different systems the following nomenclature is adopted. The different sub-systems are labeled with the index i. The different heat powers applied to each sub-system are labeled with j.

$i = 1$: Photon Stop Thermal Shield $j = 0$: 0 Watt
$i = 2$: Cryostat Thermal Shield $j = 1$: 25 Watt
$i = 3$: Beam Screen $j = 2$: 50 Watt
$i = 4$: Cold mass $j = 3$: 10 Watt

Equation (1) then becomes:

$$Q_{ij} j = \dot{m}_{ij} \cdot C_p \cdot \left(Tout_{ij} - Tin_{ij} \right). \tag{3}$$

Step 1: Nominal condition

Step 1 consists in estimating the heat load with method #1 (see chapter 3.1). Once the conditions were fixed (mass-flow, temperature as in Table 1), 40 minutes to 2 hours waiting period was required to allow the system to reach equilibrium.

Figure 10 shows the evolution towards the initial thermal equilibrium. Figure 11 illustrates a snapshot of the ACNET interface used to monitor the experiment. This snapshot was taken at the start of the measurement (at the so-called nominal conditions). The difference of temperatures between the inlet and outlet of each sub-system can be extracted to derive the static heat loads.   These temperature differences (together with all the other vital parameters, such as the mass-flows) can more easily be extracted from the ACNET F9 summary pages (Figure 12).

As a result of step 1, we can define the static heat load, Q_{10} in this case (Case B: i=1, j=0) to be (C_p~5.2 J/g-K): $\dot{m}_{1,0} = 1$ g/s, $Tin_{1,0} = 79.38$ K, $Tout_{1,0} = 82.58$ K. Hence, according to equation 3 the static heat load on the photon stop thermal shield (i=1) in the case B is $Q_{10} = 16.64$ W.
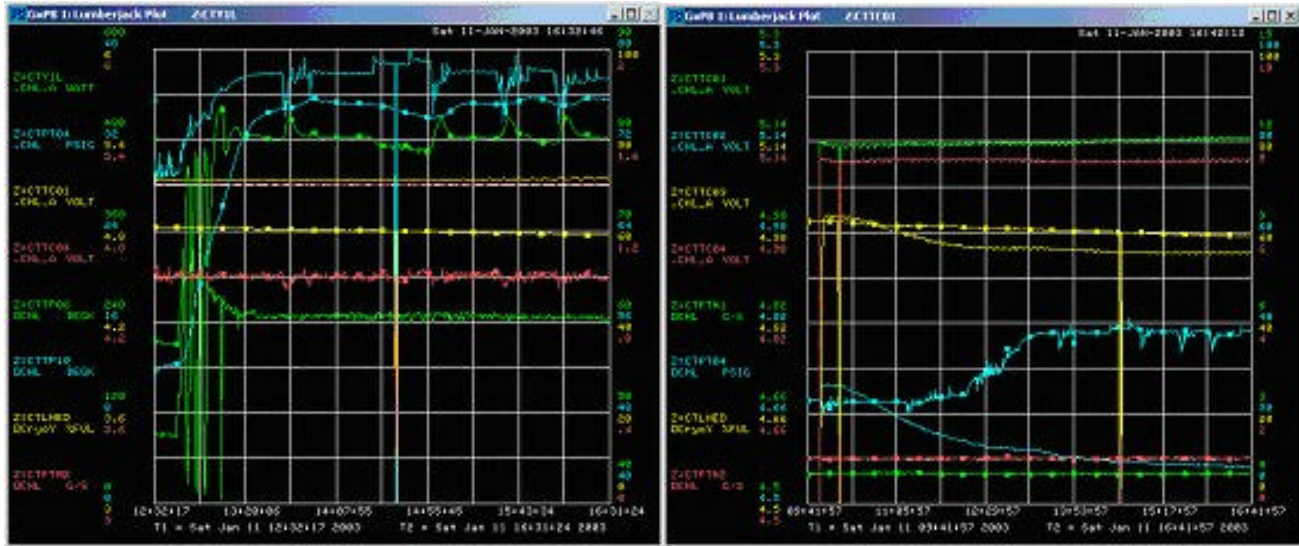

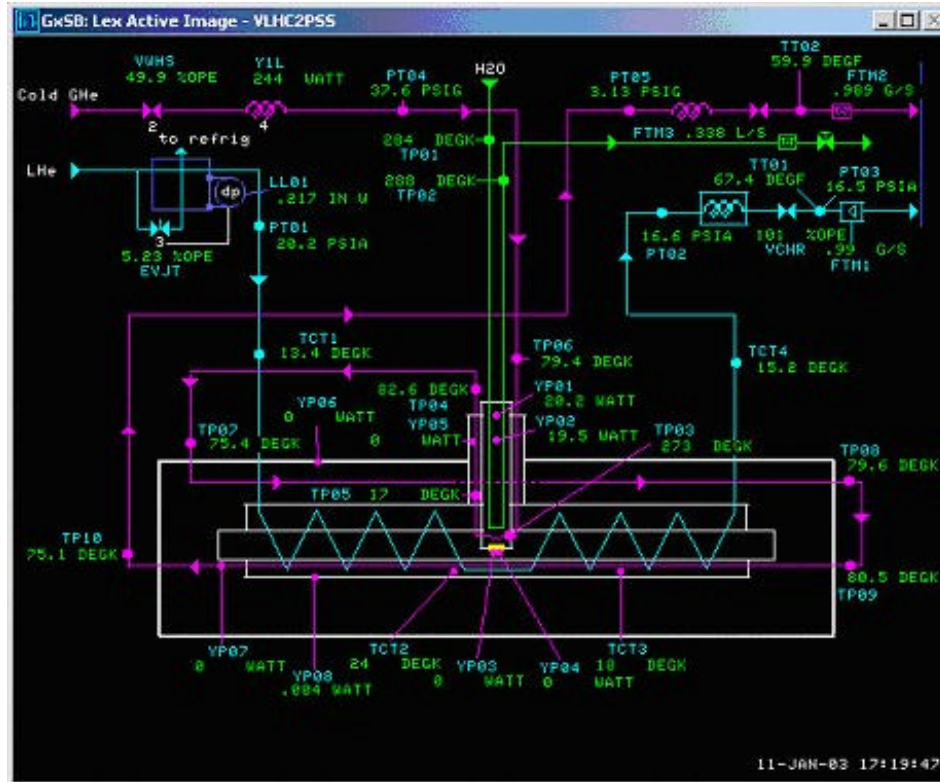Figure 10: Temperatures evolution for the nominal condition

Figure 11: ACNET interface showing nominal condition – case B.

Figure 12: Set of F9 pages at case B nominal condition

Step 2 – Applying electrical load on sub-system i

In a second step the residual heat load is measured with the heater method, as described in 3.1. The heater of sub-system i, is powered according to j = 1/2/3 (25 W /50 W /10W). The mass-flow must remain constant during this operation as the system evaluates towards the next thermal equilibrium. The APACS system maintains the flow to within ~1%. The time constant to reach thermal stabilization is of the order of 10-20 min. At the end of this time, snapshots of the temperature and other parameters are recorded as in step 1 (Figure 11 & Figure 12). In this case, i=1, j=1 (24.9 W), $\dot{m}_{1,1} = 1.02$ g/s, $Tin_{1,1} = 78.82$ K, $Tout_{1,1} = 84.77$ K and the static heat load on the photon stop thermal shield in the case D is $Q_{11} = 31.56$ Watt.

Step 3 – Increase electrical load on sub-system i

The heater of sub-system i, is powered to 50 Watt (j=2). Data are handled just as for step 2. Then we repeat the sequences for j=3. Case B: i=1, j=2 (49.66 w), $\dot{m}_{1,2} = 0.995$ g/s, $Tin_{1,2}$ = 78.19 K, $Tout_{1,2}$ = 87.53 K. The static heat load to the photon stop thermal shield now is Q_{12} = 48.32 Watt.

Step 4 – Extrapolation to the residual heat load

After step 3 we have data for three heat loads attributed to the applied electrical power j=1, 2 and 3. Figure 13 shows a plot of the measured heat load on the photon stop thermal shield together with an example of the extrapolation to the residual heat load. In the case B, a third electrical power was not used. In the case B, the residual heat load to the photon stop thermal shield obtained by extrapolation is Q_1 = 14.7 Watt. Hence, the extrapolation is obtained on the basis of Q_{11} and Q_{12} only. The table adjacent to Figure 13 also summarizes the measured heat loads in the other systems, comparing the results obtained with the two methods of measurements. The discrepancy between the results obtained with the different methods is discussed in further detail in chapter 3.5).

Extrapolation of the heat load with method 2

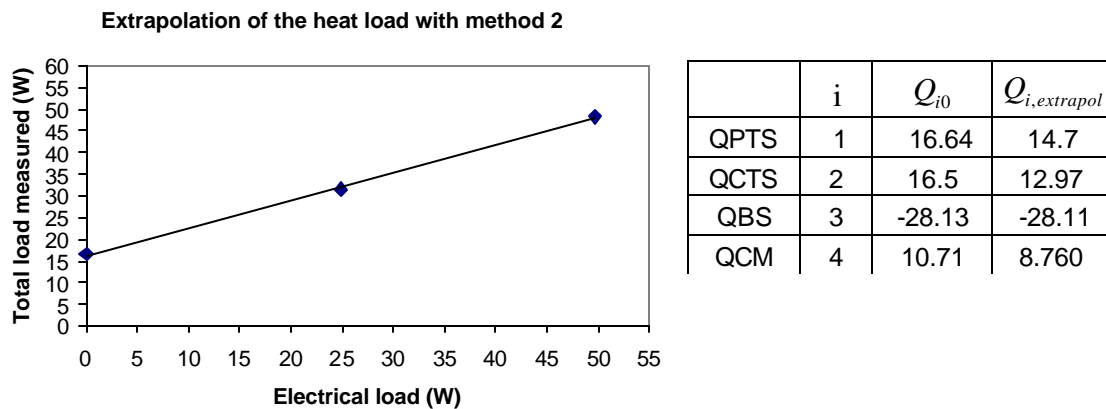|	i	Q_{i0}	$Q_{i,extrapol}$
QPTS	1	16.64	14.7
QCTS	2	16.5	12.97
QBS	3	-28.13	-28.11
QCM	4	10.71	8.760

Figure 13: Example of measured heat load on the photon stop thermal shield in case B as a function of applied heater power and extrapolation to the residual heat load.

Step 5

Steps 1 to 4 are repeated for the other sub-systems i=2, 3 and 4. The table in Fig. 13 summarizes the results.

Conclusion

The following diagram summarizes the procedure used to calculate the different heat loads in the system. Figure 15 shows the temperature evolution along the cold helium circuit during a measurement (case H, see Table 3 in 3.4). As explained in chapter 3.3, the first step consists in powering the dummy cold mass heater to 15 Watt. After 10-20
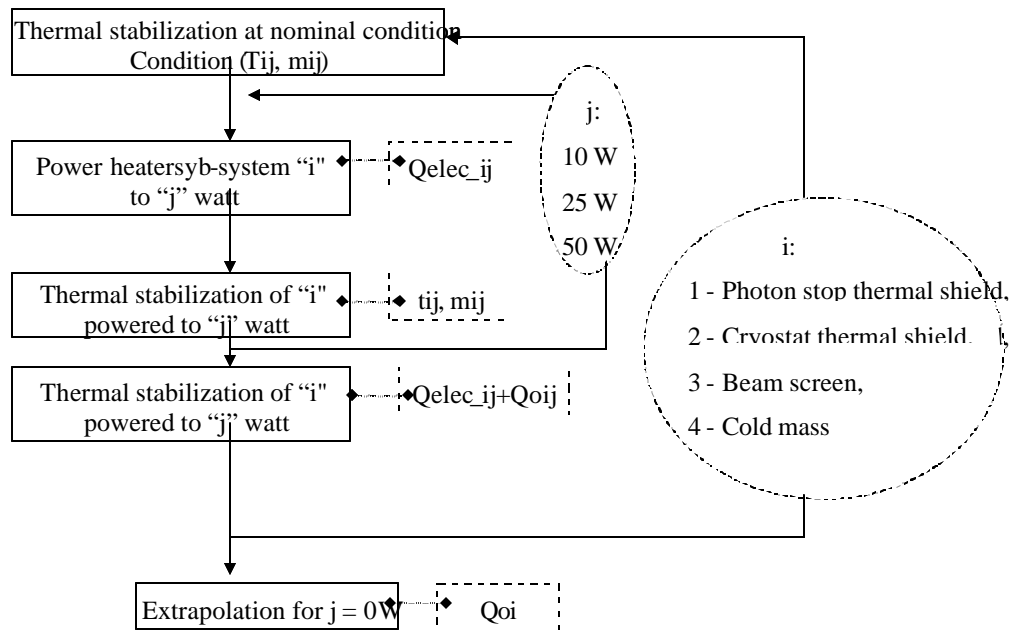
Figure 14: Photon stop test procedure diagram.

minutes, the warm end of the cold mass (TCCMOU) achieved the new temperature equilibrium.   The goal was to measure the temperature difference between the inlet (TCCMIN) and outlet (TCCMOU) of the cold mass cooling tube for different electrical powers applied to the cold mass system, as explained in chapter 3.1.   As expected the temperature at the inlet of the dummy cold mass cooling spiral (TCCMIN) remained constant when the heater was powered (indicating that the flow of helium was sufficient for this test). Figure 15 and Figure 16 show examples of the temperature evolution
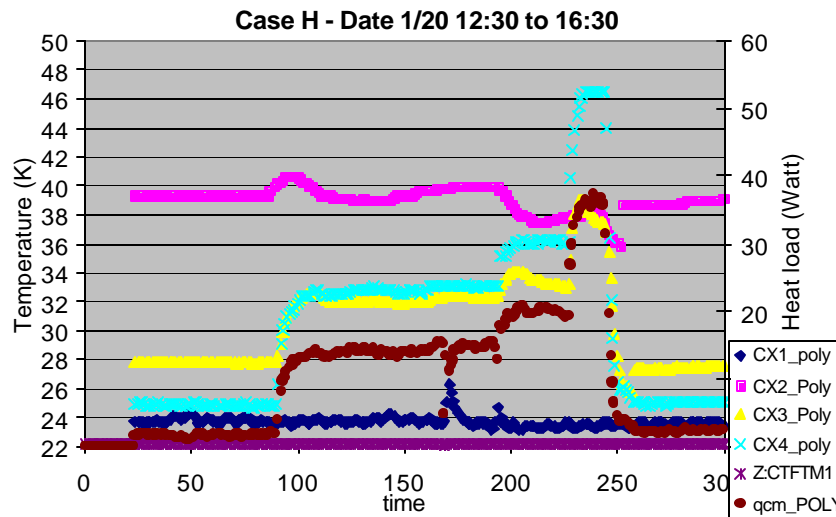

Figure 15: Temperature stabilization of the cold helium loop for case H (time in min). CX1-CX4 are the Cernox sensors affixed to the dummy cold mass. Qcm_poly is the measured residual heat load (referring to the right ordinate). The application of three different heater powers can be clearly seen.
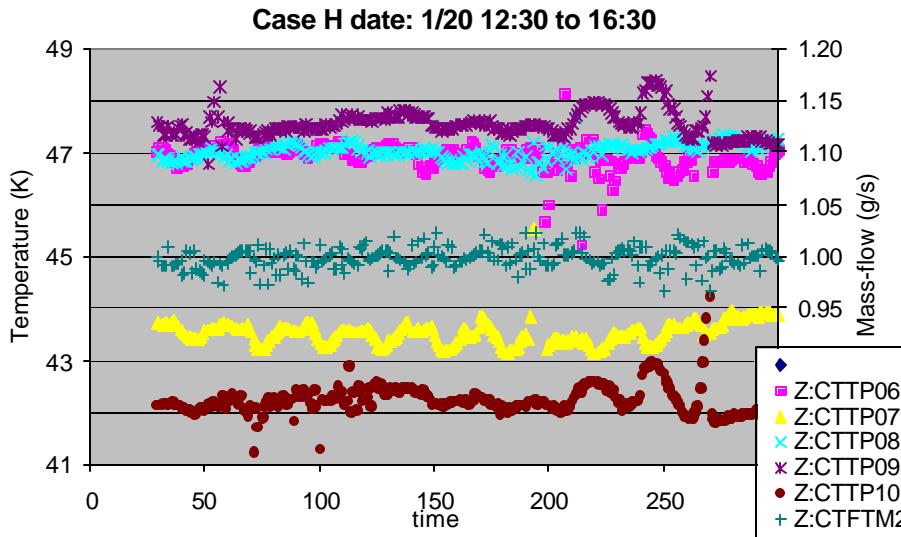
Case H date: 1/20 12:30 to 16:30

Figure 16: Temperature distribution along the warm helium loop for case H (time in min). CTTP06-CTTP10 are the different Pt temperature sensors mounted along the warm helium loop. The mass-flow sin the warm helium loop is shown also (CTFTM2 – referring to the right ordinate).

during one of the experimental cases in the cold and warm helium loops (see Table 3). Figure 15 clearly shows the increase in temperature of the cryogen (see sensor TCCMOU vs TCCMIN) with the three different applied heater powers. Figure 16 shows that all sensors on the warm helium loop are unaffected by the heat deposited on the cold mass with the YCM heater. This proves that the heater measurement technique was sound.

3.4) Summary of all Test Cases

Table 3 contains a summary of all the test cases studied. The different cases represent different operating conditions. Some cases had to be removed: case A, being the first run, generated unusual results. It was therefore removed, given that the confidence level for this first measurement was low. Case C had to be eliminated because measurements were taken before thermal equilibrium had been achieved. The major differences between these cases are in: 1) the cold helium loop temperature / mass-flow between ~15 K / 1 g/s (B,F,G and K) and ~25 K / 0.3 g/s (D,E,H,I and J); 2) the warm helium loop temperature between 50 K such as in the cases D,E,H,I,J and K and 75 K, such as in B,F and G; 3) the mass flow in the warm helium loop between 0.3 g/s (B,D,E,H,I,J and K) and 5 g/s (F,G); 4) the temperature of the photon stop nose between ~270 K (B,D,F,H) and ~370 K (E,G,I). In cases J and K the water circuit was cooled with liquid nitrogen to ~85 K to add an additional low temperature point in the heat load vs. photon stop temperature graphs.   The temperatures quoted in the table are the average temperatures computed from the inlet and outlet values in each respective circuit in the so-called initial conditions (that is without additional heater power deposited in them). The order of the columns related to the shield circuit (photon stop thermal shield – cryostat thermal shield – beam screen) in Table 3 reflects the direction of the cryogen flow. As it is discussed

further in a later section of this document the temperature sensor readings are believed to have been affected by direct heating from accidental, spurious heat sources. Therefore, the temperatures quoted in the table are not consisted with the direction of the flow. The flows quoted in the table are typically averages of ~10 measurements over the duration of the entire measurement in each case. As discussed in appendix D, the temperature was stable within a measurement to less than 0.2 K.

Table 3: Summary of the parameters in all experimental cases of the photon stop test. Cases A and C were removed (see text for reasons).

	Cold mass	Cold mass	PS shield	Cryostat shield	Beam screen	80 K shields	PS water	PS nose	Water circuit
	Temp (K)	Flow (g/s)	Temp (K)	Temp (K)	Temp (K)	Flow (g/s)	Temp (K)	Temp (K)	Flow (g/s)
CASE B	14.64	0.977	80.98	77.00	76.11	1.008	286.00	271.00	0.35
CASE D	23.59	0.296	48.41	45.15	44.97	1.034	286.10	271.00	0.35
CASE E	22.29	0.307	49.35	44.97	45.44	1.010	312.50	360.00	0.35
CASE F	14.37	1.060	75.32	72.52	71.08	5.021	286.25	271.00	0.35
CASE G	15.20	1.026	77.03	72.01	71.74	4.997	326.20	376.00	0.35
CASE H	24.54	0.323	48.42	44.88	44.80	1.007	286.25	271.00	0.35
CASE I	25.13	0.299	49.82	45.81	45.70	1.017	321.15	377.00	0.35
CASE J	24.00	0.302	45.44	43.46	43.37	0.998	86.37	83.00	-
CASE K	13.08	1.006	45.68	43.53	44.15	1.062	86.32	85.00	-

3.5) Results

The following general observations were made:

1. As expected the photon stop temperature affects every other circuit, i.e. the residual heat load measurements on the cold-mass as well as the shield circuits indicate an increase of the static heat load with the photon stop absorber temperature. Plots of the residual heat load measurements on the most important sub-systems, the cold-mass, photon stop thermal shield and beam screen are shown in Figure 18, Figure 20, Figure 21.

2. When the thermal shield circuit temperature is varied between ~45 K and ~80 K the cold mass residual heat load increases 5-fold, as well more or less as expected. Figure 19 shows a plot with the residual cold mass heat load as function of the shield temperature.

3. When the temperature in the cold mass circuit is reduced from ~25 K to ~15 K, the residual heat load increases ~5-fold, more or less as expected (Figure 18).

The measurements, however, indicate residual heat loads on all circuits that were larger than expected (see Figure 18-Figure 21). Then, the temperature readings in the warm helium loop (shield circuit) were not consistent. In some cases (see Figure 21) the temperatures decreased along the direction of the flow. This effect clearly appears in Table 3, which lists the average (between inlet and outlet) temperature in the three shields, which are supplied in series (and which therefore increase instead of decrease in the order of flow). Also the Cernox temperature readings on the cold helium loop were

not as expected, with sensor 2 (TCCMMI) reading ~10 K higher values than the other sensors (and not changing as substantial heat was supplied to the cold mass). The following lists the issues that have been identified (chapter 4 discusses some of the procedures used in this process):

1. It appears that spurious heating was introduced into the system by un-shielded water supply-tubes and/or an insufficient cooling of the cryostat thermal shield. This is evidenced by the stronger than expected effect of the water and shield temperatures on the cold mass residual heat load. The total heat radiated from the water tubes at 270 / 370 K is ~ 12 / 42.4 W! The total heat radiated by the cryostat end-caps, assumed to be at 100 K is ~0.3 W.

2. The biggest problem, however, is to explain the seemingly inconsistent behavior of the temperatures. On the dummy cold mass, for example, the temperature sensor TCMMI, placed on the center of the cold mass as shown in Figure 17, was indicating ~10 K higher temperatures than the other sensors and was not affected by activation of the cold-mass heater (which was placed at the input end of the cold mass tube). If the temperature sensor reading is accurate, one has to assume that the cooling of the cold mass was insufficient. Similar assumptions have to be made for the beam screen and the cryo-stat thermal shield (see point 1), which in turn explains increased heat-load from these sources.

3. Furthermore, if 1) is true, than direct heating of the sensors could also have resulted in over-estimating heat loads. A calculation of the temperature rise produced on a Cernox sensor by the radiation emitted from the water tubes indicates a 0.4 K / 1.4 K effect with water temperatures of 270 and 370 K. It is possible that the TCCMOU Cernox sensor on the cold helium loop was exposed to this heating. All Platinum sensors most likely were exposed. Efforts, however, to reconstruct their real temperature on the basis of either calculations of the direct sensor heating or calculations based on a comparison of measurements in similar conditions but different flow-rates (such as cases B and F) were not successful. These temperature offsets due to direct heating of the sensor are believed to be the reason why some heat loads in the shield circuit were negative (outlet temperature colder than inlet temperature). The fact that the real temperatures could not be reconstructed made it difficult to interpret the measurement results for the shield circuit residual mass. They were therefore not considered further here. Figure 21 shows the case of the heat load on the beam screen, which rises as expected with the temperature on the photon stop tip, but features negative heat loads.

4. The analysis of the experimental data possibly hints toward the occurrence of a direct conductive contact between beam screen and cold mass as well as between the photon stop insert and the photon stop thermal shield. The former could be the result of sagging of the beam screen assembly under the weight of the photon stop. The latter could be the result of a build-up of insulation material (associated with safety heaters) beyond the allowed thickness given by the ~1.5 mm gap between the photon stop insert and the shield. Thermal contraction of the shield could also have played a role.
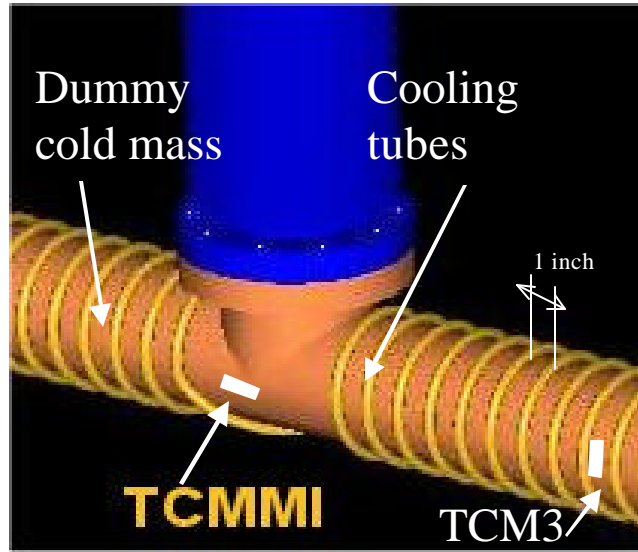
Figure 17: Location of sensors TCMMI and TCM3 on the cold bore assembly.

Regarding the measurement technique it was observed that, in some cases, a 20% disagreement between the residual heat loads derived from the two techniques was found. Table 4 shows a comparison of the measurements of the dummy cold mass heat load with both methods. It is believed that this discrepancy was partly caused by the fact that the chosen heater power was much higher than the residual heat load, therefore reducing the precision of the data extrapolation. Also, in the case of the dummy cold mass, for example, the heater was placed close to the outlet rather than close to the inlet. The heater therefore directly heated the TCMMOU sensor, thus falsely indicating a larger residual heat load. In the case of the beam screen heater, for example, it was found that the heater was close enough to the cold helium supply tube to heat the incoming helium loop in the cooling circuit. In the following the data computed with the static method have been retained.

Table 4: Comparison of residual heat loads in case B as measured with both methods (static and heater method).

	i	Q_{i0}	$Q_{i,extrapo}$
QPTS	1	16.64	14.7
QCTS	2	16.5	12.97
QBS	3	-28.13	-28.11
QCM	4	10.71	8.760

The following plots show some of the major results of the measurements before correction for the above mentioned issues. Figure 18 shows the main result plots for the dummy cold mass. The measured residual heat load on the cold mass is plotted against the temperature on the photon stop nose. All cases listed in Table 3 are included. Also shown is the (calculated) expected behavior. The photon stop design was such that no correlation was expected between photon stop temperature and the cold mass heat load (a weak, indirect correlation, however, was anticipated as a result of heating of the beam screen and the conduction between the beam screen and the cold mass via the spiders). The measured heat load, in fact, shows a correlation, which suggests the existence of additional heat load components, possibly of the radiation type. More details on the model and possible
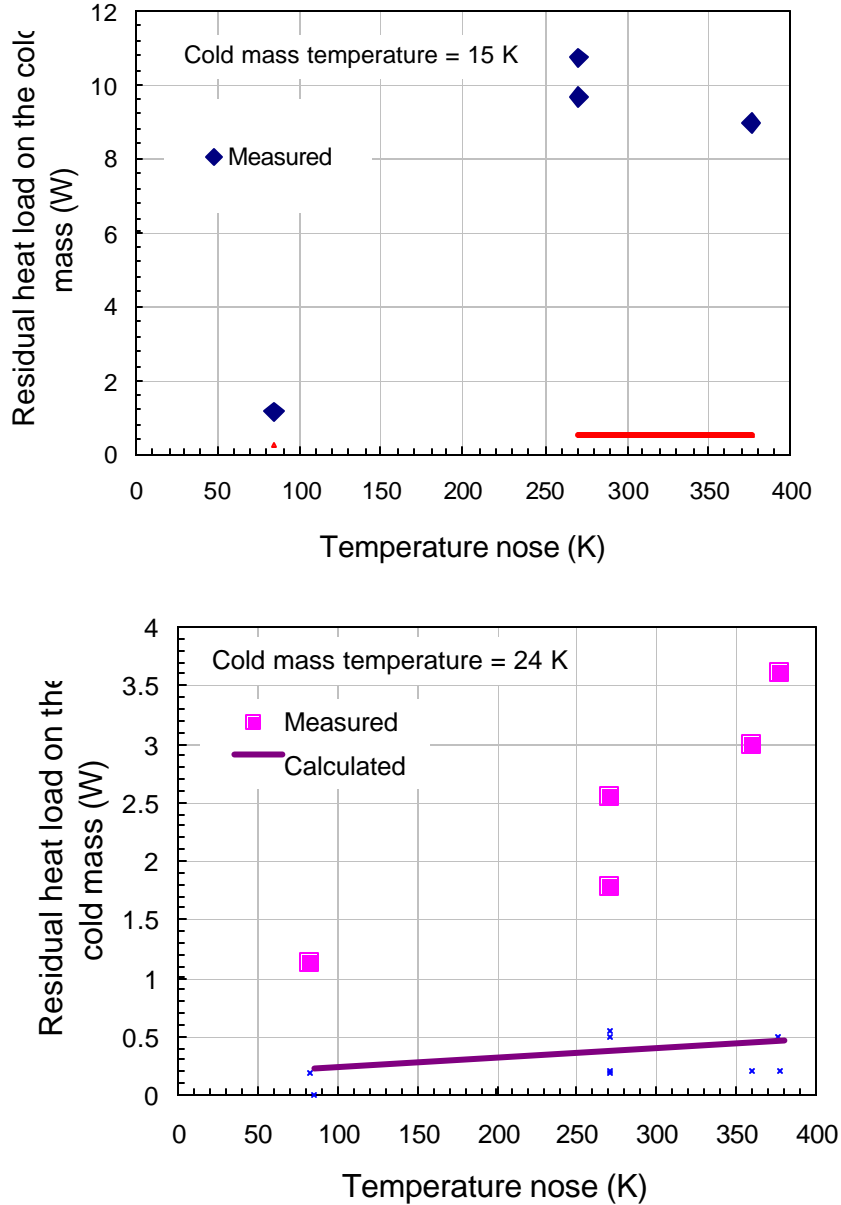
Figure 18: Residual heat load on the cold mass as a function of photon stop nose temperature at a cold mass temperature of 15 K (top) and 24 K (bottom). Calculated data are as expected according to the design model (see chapter 4 for further discussion).

explanations are discussed in chapter 4. The plot clearly shows that the goal to limit the residual heat load on the cold mass system to less than 1 W could not be achieved in this experiment. As will be discussed in further detail in chapter 4 we believe that this is the result of "accidents" rather than the result of an inadequate design. A similar discrepancy was found between the expected and measured dependency of the cold mass heat load on the shield temperature (Figure 19). The only expected heat load was conduction through the G10 separating the cold mass from the beam screen. Also, the residual heat load measured on the other systems was larger than expected. See for
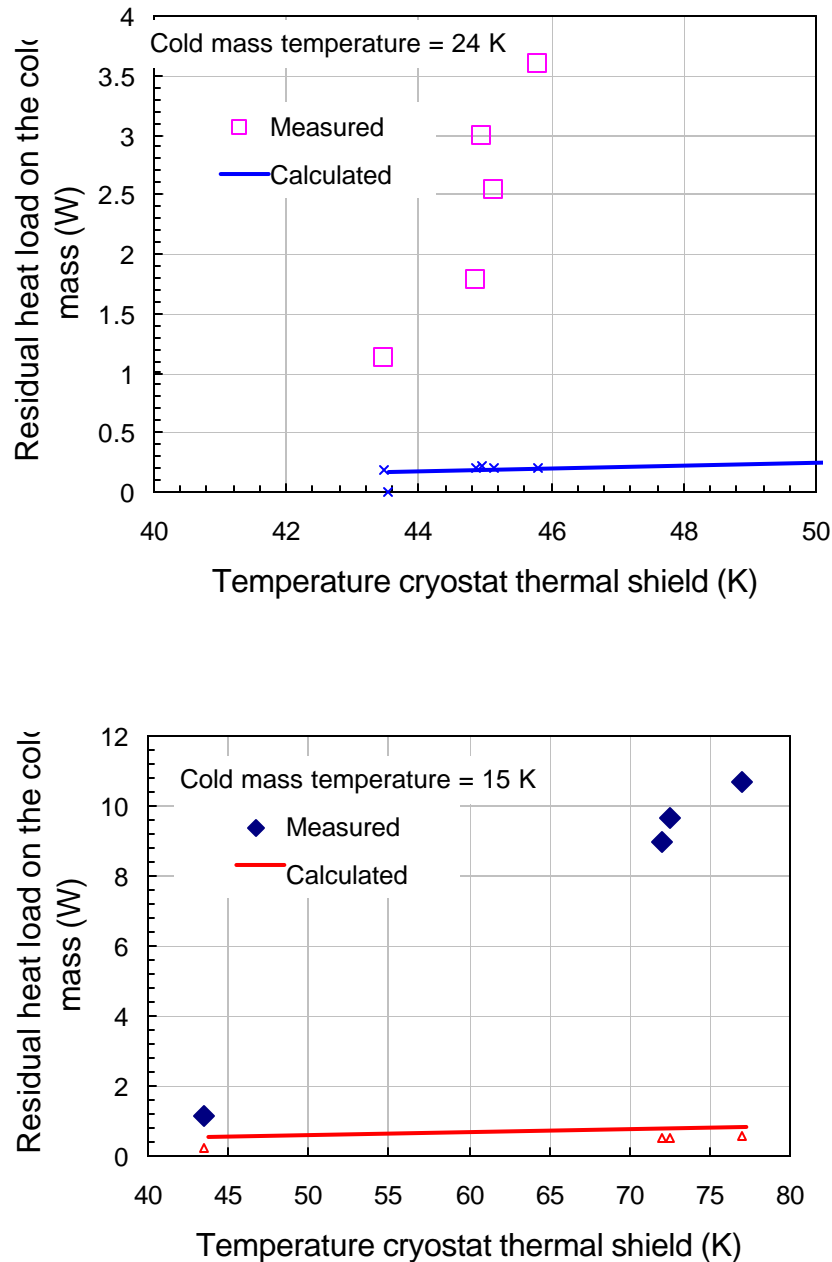
Figure 19: Residual heat load on the cold mass as a function of (cryostat, photon stop and beam screen) shield temperature at a cold mass temperature of 15 K (top) and 24 K (bottom). Calculated data are as expected according to the design model (see chapter 4 for further discussion).

example the residual heat load on the photon stop thermal shield as a function of the nose temperature (Figure 20). The expected modes of heat transfer were 1) radiation from the hot photon stop to the surrounding shield; 2) conduction through the three G10 pins at the bottom of the photon stop; and 3) conduction from room temperature through the top bellows. A similar plot for the heat load as a function of the photon stop temperature measured on the beam screen is shown in Figure 21.
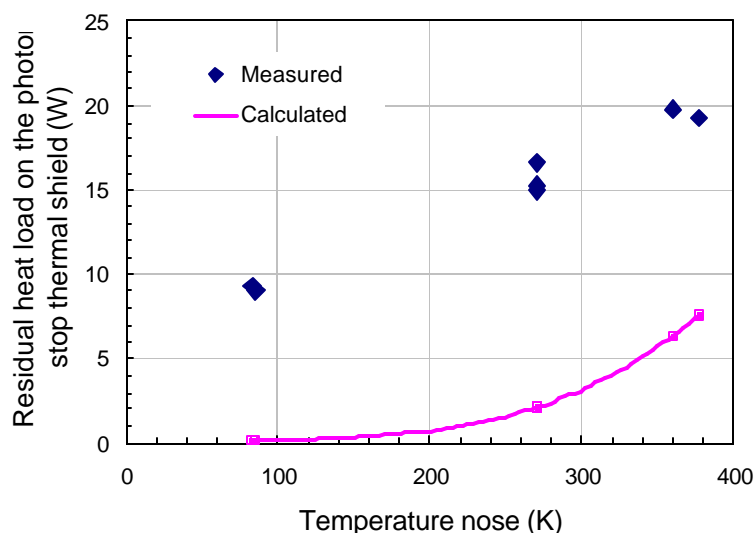
Figure 20: Residual heat load on the photon stop thermal shield as a function of photon stop nose temperature. Not shown explicitly are the temperatures of the photon stop thermal shield (they vary between 45 and 80 K according to the case – see Table 3). Cases F&G gave much larger heat loads and were removed from the shown dataset. It is possible that the large flow (5 g/s) in the shield system resulted in unstable conditions.. Calculated data are as expected according to the design model (see chapter 4 for further discussion)
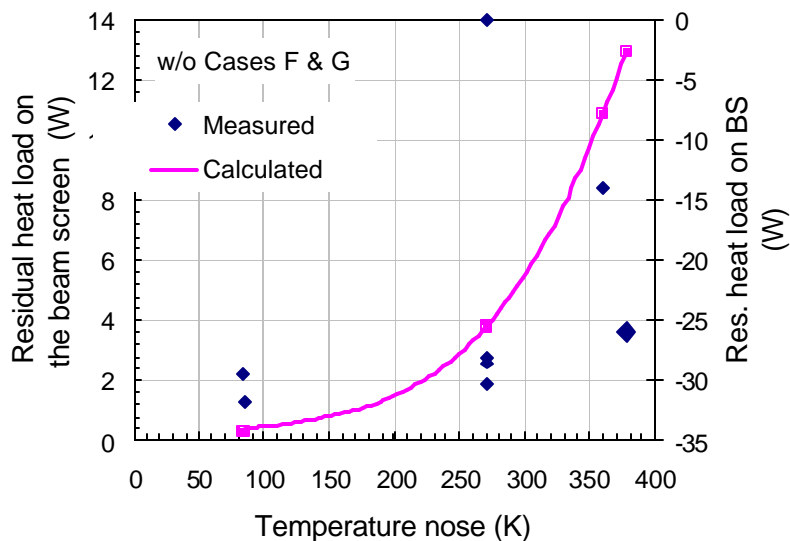

Figure 21: Residual heat load on the beam screen as a function of photon stop nose temperature. Not shown explicitly are the temperatures of the beam screen (they vary between 45 and 80 K according to the case – see Table 3). Cases F&G gave much larger heat loads and were removed from the dataset shown. It is possible that the large flow (5 g/s) in the shield system resulted in unstable conditions. Note that temperature offsets in the Pt sensors are the cause for negative heat loads (see right ordinate). The calculated data were therefore plotted on a relative scale. Calculated data are as expected according to the design model (see chapter 4 for further discussion).

4) MODELING AND ANALYSIS

4.1) Photon Stop Thermal Model

As explained above the need arose to understand the discrepancy between the expected and measured residual heat loads in the photon stop system. We believe that the discrepancy is the result of some accidents resulting in the introduction of spurious heat sources into the system. The following discusses the models that were used to predict the heat loads on the various systems as well as the extension of the thermal model to include the external, accidental heat sources. The extension of the model was guided by a powerful multi-parameter optimization that allowed determination of the model parameters that fit best the experimental data. In an iterative process, additions and refinements were made to the model until the optimization algorithm generated a reasonable set of values for the model parameters. It has to be mentioned that there is no guarantee that this process led to the real experimental circumstances. There is, however, no doubt that the lack of shielding of the water-tubes and insufficient cooling of the cryostat thermal shield introduced large amounts of heating power, 10 or more times larger than the system design heat load.

The schematic in Figure 22 shows the thermal model that was finally adopted to describe the photon stop experiment. The model includes all expected heat transfer mechanisms as well as the accidental heat sources. The expected / unexpected paths of heat transfer are traced with bold / dashed lines. The different temperature levels are grouped from left to right in the schematic. At more or less room temperature are: the photon stop insert and the water tubes, which were left unshielded (i.e. with MLI). The shield circuit (cryostat thermal shield, photon stop thermal shield and beam screen) operated at an intermediate temperature (~50-80 K). The cryostat thermal shield is mainly receiving thermal radiation from the outer, room temperature walls of the cryo vacuum-vessel. The vacuum vessel thermal shield consists of a copper shield, cooled with a cooling spiral containing the cold helium gas, and surrounded by a wrap of 30 layers of MLI. Radiation and conduction into residual gas were neglected (the pressure in the cryostat vacuum was 10^{-6} mbar). The photon stop inner shield absorbs mostly the thermal radiation from the room temperature photon stop insert, which it surrounds. The photon stop insert is not free-floating within the inner shield, rather it is spread from the shield through a guiding support consisting of three G10 pins, ~2 mm in diameter, press-fitted into the nose-piece (at the bottom) of the photon stop insert. The G10 pins contribute to conduction from the absorber to the inner shield. The annular gap between the insert and the inner shield is nominally 1.65 mm. It is believed that this gap was insufficient and that some direct contact was introduced between the photon stop insert and the shield via build-up of insulation material due to the safety heaters and the thermal contraction of the cold photon stop thermal shield. Furthermore, the inner shield receives heat via conduction through the inner shield top bellows, which are at room temperature on the top. The dummy beam screen absorbs the radiation from the ~350 K photon stop tip as well as some of the heat conducted through the G10 centering pins. The dummy cold bore is operated at ~15 K by running liquid helium through the cooling spiral. It obviously received more radiation than expected from the cryostat thermal shield and the dummy beam screen. The largest heat load contribution, however, was expected to occur
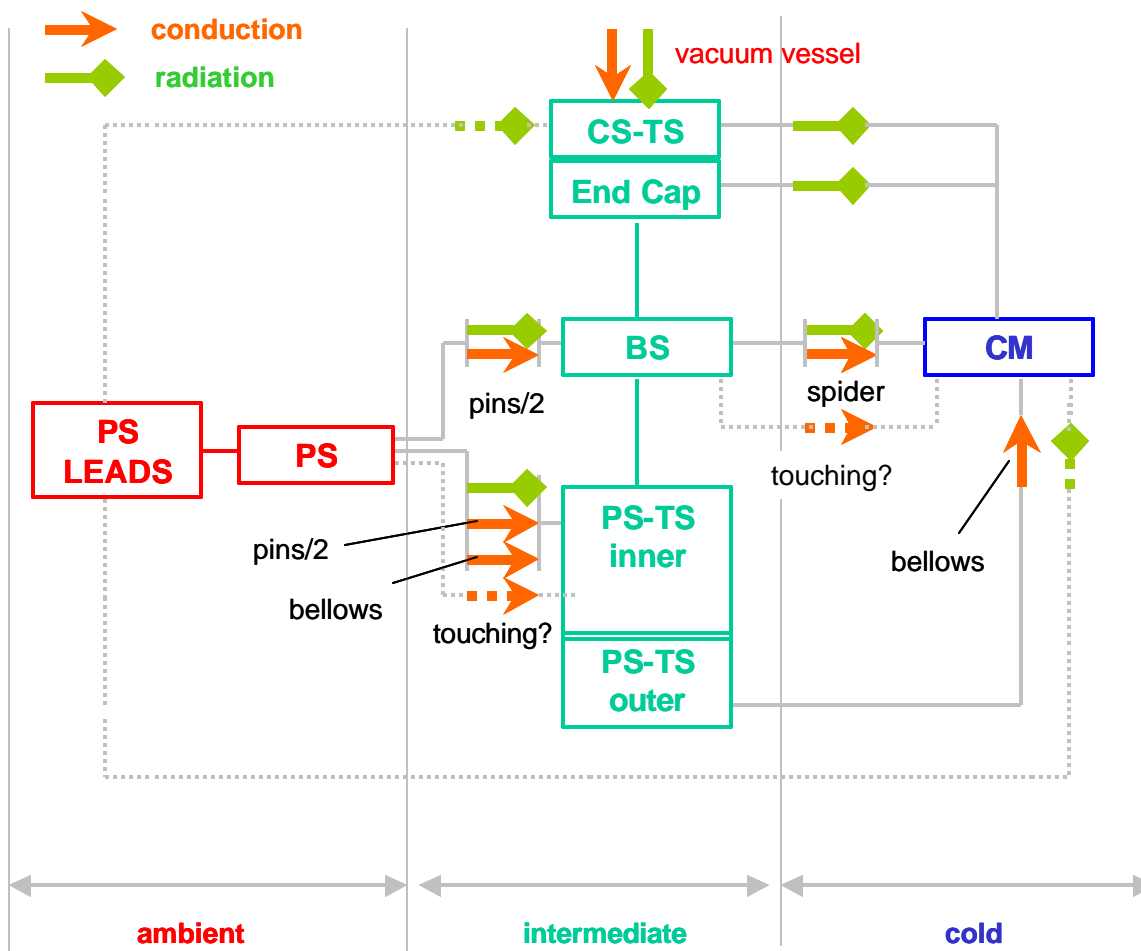
Figure 22: Photon stop model diagram. The diagram is grouped into three classes, ordered from left to right, representing the three different temperature stages. All possible conductive and radiation heat transfer paths between the different photon stop components are shown. The "accidental" transfer paths are indicated with dashed lines. Nomenclature: PS...photon stop, CS-TS…cryostat thermal shield, BS...beam screen, PS-TS...photon stop thermal shield, CM...cold mass.

via conduction from the beam screen via the support spiders. Some additional conduction was expected to occur through the outer photon stop shield bellows, which are at the shield temperature on the top.

The accidental heat sources found to be significant are: 1) radiation from the unshielded water tubes leading from a flange on the side of the cryostat to the top of the photon stop; 2) possibly a mechanical contact between the beam screen and the cold-mass due to a sag of the cold-bore beam screen assembly caused by the weight of the photon stop; 3) possibly touching of the photon stop and the photon stop thermal shield due to an excessive build-up of Kapton™ on the photon stop insert (safety heaters!). In addition, and not particularly outlined in the schematic (because expected), there is the possibility of increased radiation from the cryostat thermal shield, which was warmer than expected due to insufficient cooling of the thermal shield. These contributions were found on the basis of a trial and error approach in which the model data were fit to the

experimental data using a multi-parameter optimization routine in Excel. The following describes the parameters and equations of the model.

The model was based on a simple set of thermal equations presented in the following. All calculations are appended at the end of this document (appendix G). The model parameters are all the conductive and radiation constants associated with the thermal links outlined in the schematic in Figure 22. The model calculates the material parameters (conductivity, emissivity, specific heat,) for each subsystem at a representative temperature (Table 5). The model also uses the real photon stop geometry, or simplified geometry models based on the real geometry (Table 6).

The thermal conductivities of the different components were calculated with (4) from the average temperature dependent thermal conductivity $k(T)$ of the material, the active length L_{therm} and thermal contact area A_{therm}.

$$C_{cond} = \frac{\int_{T_{cold}}^{T_{warm}} k(T)dT \, \frac{A_{contact}}{L_{therm}}}{(T_{warm} - T_{cold})} \qquad (W/K) \tag{4}$$

The radiation type correlations were described with equation (5)

$$Q = C_{rad}\left(T_{warm}^{4} - T_{cold}^{4}\right) \qquad (W) \ , \tag{5}$$

where the geometrical constant C_{rad} is calculated from the cold and warm surfaces A, the Stefan-Boltzmann constant and the emissivity of the warm surface e_{warm}.

$$C_{rad} = 5.67 \cdot 10^{-8}\left(\frac{W}{m^{2}K^{4}}\right) \times A_{cold}\left(m^{2}\right) \times \frac{1}{\left[\frac{1}{e_{warm}} + \frac{A_{warm}}{A_{cold}}\left(\frac{1}{e_{cold}} - 1\right)\right]} \qquad \left(\frac{W}{K^{4}}\right) \tag{6}$$

As can be seen in appendix G the emissivity of the copper surfaces (cold mass, cryostat

Table 5: Summary of the temperatures used to calculate emissivities and heat conductivities for the parameters used in the photon stop model calculations (Table 7). The temperatures are more or less typical of the conditions in the photon stop experiment.

Temperature of the cold bore (K)	19
Temperature of the beam screen (K)	80.5
Temperature of the cryostat thermal shield (K)	79.5
Temperature of the photon-stop (absorber) (K)	273
Temperature of photon stop, inner shield (K)	78.5
Temperature of vacuum vessel (K)	300

Table 6: Geometry parameters in photon stop model.

Vacuum vessel (cryostat)	
Vacuum vessel cylinder length / diameter / radiating surface	1.753 m / 0.508 m / 2.797 m^2
Cryostat shield supports: thermal length / conduction surface (8 blocks)	0.114 m / 8 x 161.3 mm^2
Cryostat thermal shield	
Cryostat thermal shield length / diameter / surface	1.524 m / 0.49 m / 2.344 m^2
End cap surface (2 endcaps)	2 x 0.2 m^2
Photon stop-absorber insert	
Photon stop-absorber insert length / diameter / radiating surface	50.2 cm / 3.48 cm / 0.055 m^2
Beam screen	
Beam screen tube length / diameter / surface	1.524 m / 3.8 cm / 0.182 m^2
Cold bore	
Cold bore tube length / diameter / surface	1.321 m / 7.6 cm / 0.316 m^2
G10 spider between beam screen and cold bore	
Thermal length / thickness/ total contact area (2 spiders, 3 contacts)	3.89 cm / 3.05 mm / 3 x 2 x 118.6 mm^2
Bellows photon stop outer shield	
Bellows diameter / wall thickness / stretched length	7.6 cm / 0.15 mm / 0.711 m
Bellows conduction surface	35.84 mm^2
Bellows photon stop inner shield	
Thermal shield tube length / diameter / absorbing surface	0.5 m / 3.8 cm / 0.055 m^2
Bellows diameter / wall thickness / stretched length	3.8 cm / 0.15 mm / 0.61 m
Bellows conduction surface	33.13 mm^2 / 61 cm
G10 pins	
G10 pin diameter / thermal length / transfer area (3 pins)	6.35 mm / 3.2 mm / 3 x 31.67 mm^2
Water tubes (leads)	
Water tube length / diameter / surface (2 tubes)	50 cm / 1.3 cm / 2 x 0.02 cm^2

thermal shield,..) were assumed to be higher than for polished copper. In fact the emissivity of Al was used (and multiplied by 2). This was necessary top account for the fact that the surfaces were not polished (but rather oxidized in some instances). Materials considered are copper and stainless steel. The thermal conductivities used are also given in appendix G.

4.2) Results of Model Calculations

Table 7 reports the estimates of these constants (C_{rad} and C_{cond}), calculated from (4) and (6), together with the values obtained on the basis of the optimization procedure, if available. These calculations were only conducted for the cold-mass residual heat loads for the reasons indicated above. Also, the measured residual heat loads were taken "face-value" and no corrections for directed sensor heating were included. Note that the parameters C_{rad} and C_{cond} were calculated at the temperatures listed in Table 5 and the geometry parameters listed in Table 6. These temperatures are typical but not always exact. For example the thermal conductivity through the small spiders between the beam screen and the cold bore, assumed a temperature difference of 81 K on the beam screen side and 19 K on the cold-bore side, a typical (but not always achieved) experimental condition. As explained above, the geometry parameters are those measured on the parts of the experimental apparatus (or calculated on the basis of simplified models of these parts). Also important is the fact that the actual temperatures of the cold mass, the

cryostat thermal shield and the cryostat thermal shield end-caps as well as the beam screen were also optimized to account for the fact that the cooling was thought to have been insufficient. Table 7 also lists the temperatures increments that have to be added to the temperatures listed in Table 5 to obtain the "real" temperatures at which these systems were operating. The comparison of the expected and found cold mass thermal model parameters clearly indicates –a- the existence of additional heat sources as discussed above and –b- reasonable agreement of the parameters for the expected heat load contributions. Figure 23 show plots comparing optimized model and experimental parameters. The agreement between model data and experimental data indicates that the model outlined in the schematic in Figure 22 is a possible representation of the experimental conditions for the case of the cold mass. Table 8 summarizes the cold residual heat load contributions calculated with the model before and after calibration on the experimental data.

Table 7: Calculated model parameters for residual heat load on the different photon stop sub-systems. The parameters C_{rad} and C_{cond} are as defined in equations (4) – (6). The expected calculated values are shown side by side with those found after extension of the model to include spurious heat sources and multi-parameter optimization. The optimization results are given in terms of multiplicative factors that have to be applied to the expected heat loads. *The following additional temperatures (to be added to the baseline values in Table 5) were also obtained from the optimization algorithm: in the case of the cold mass: +4 K, beam screen and cryostat thermal shield: +10 K and cryostat thermal shield end-caps + 20 K to account for insufficient cooling of these systems and the fact that the temperatures quoted in Table 5 were measured on the cooling tubes rather than on the objects.

Heat load to cold mass	Calculated w/out "accidents"	Calculated With accidents	Multiplier found from fit of data	Comment
Radiation				
From cryostat thermal shield	2.268E-09	2.268E-09	30*	not sufficiently cooled
From beam screen	1.194E-09	1.194E-09	2*	not sufficiently cooled
From end cap	1.315E-09	1.315E-09	7*	not sufficiently cooled
From water leads	0	1.000E-09	0.5*	29% of cold-mass exposed
Conduction				
From beam screen via spider	5.000E-03	5.000E-03	2*	
From cryostat thermal shield via bellows	2.760E-04	2.760E-04	10*	touching due to "sag"?
Heat load to photon stop shield				
Radiation				
From photon stop	3.580E-10	3.580E-10	N/A	full length of photon stop
Conduction				
From photon stop via bellows	6.695E-04	6.695E-04	N/A	
From photon stop via G10 pins	9E-3	9E-3	N/A	½ of pin conduction
Heat load to cryostat thermal shield				
Radiation				
From vacuum vessel	4.49E-10	N/A	N/A	30 layers of MLI
Conduction				
From vacuum vessel via spider	7.000E-03	N/A	N/A	
Heat load to beam screen				
Radiation				
From photon stop	5.97E-10	N/A	N/A	½ of beam screen exposed

Conduction

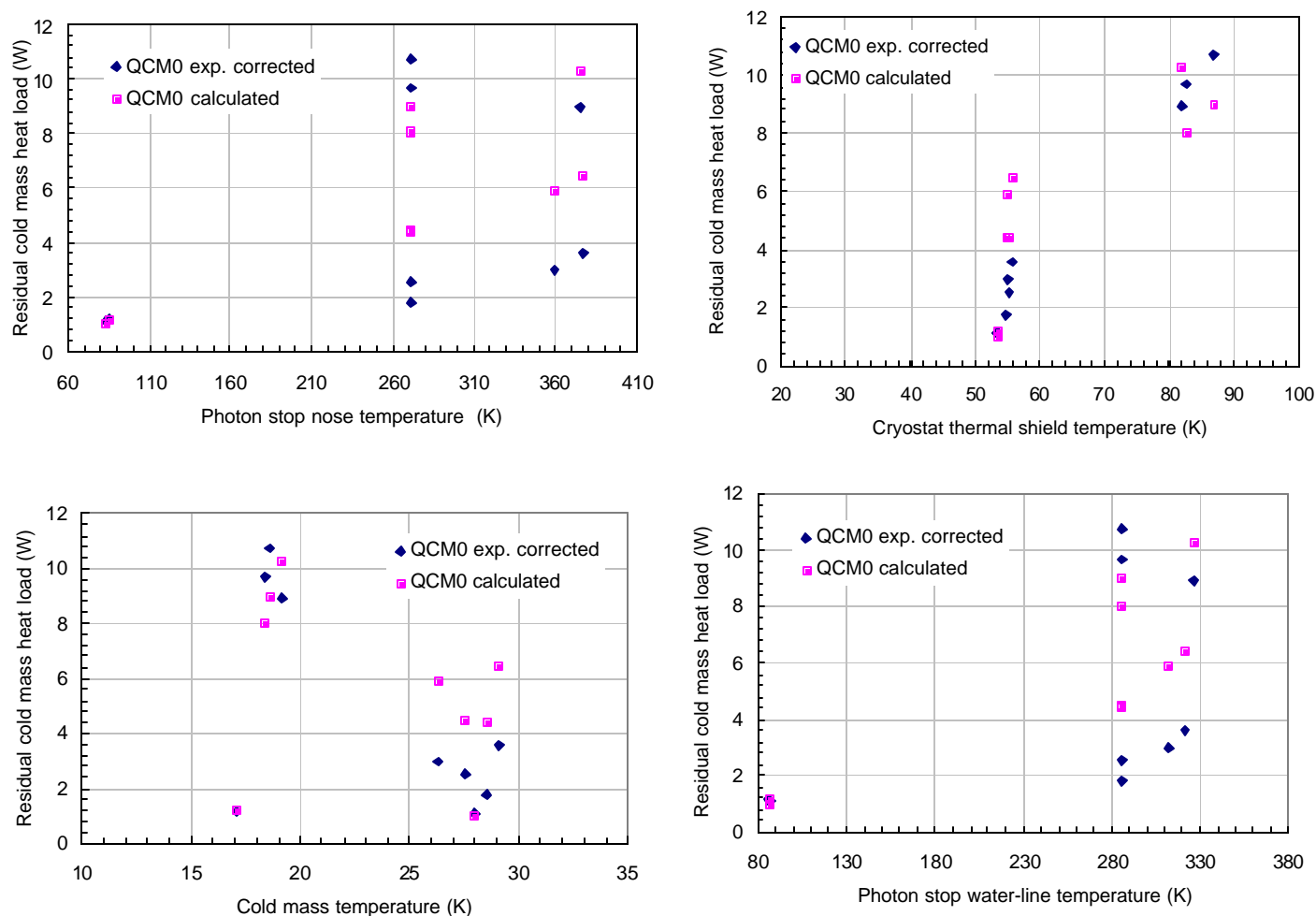|				
From photon stop via G10 pins	9E-03	N/A	N/A	½ of pin conduction

Figure 23: Comparison of experimental and calculated residual heat loads on the cold mass. The calculated heat loads were obtained with the optimized model parameters discussed in Table 7.

Table 8: Summary of the calculated expected cold bore heat load contributions (see model in appendix G) and calculated heat load contributions using the multipliers listed in Table 7 obtained from the multi-parameter fit of the experimental data.

Contributions to the residual heat load on cold bore	expected, calculated (W)	fit to experiment (W)
Radiation from cryostat thermal shield	0.09	2.7
Radiation from beam screen	0.05	0.1
Radiation from cryostat end-caps	0.17	1.19
Conduction from beam screen through spider	0.8	1.6
Conduction from thermal shield through bellows	0.02	0.2
Radiation from unshielded water tubes	0	3.32
Sum of calculated contributions	**1.13**	**9.11**
Cold mass residual heat load experimental case B (W)	**10.71**	

5) SUMMARY AND CONCLUSIONS

The first photon stop cryo test was conducted successfully during December 2002 and January 2003. Some issues hindered the test in the initial phase of the experiment, such as a leaking valve, which led to freezing of water and subsequent bursting of the photon stop. Following the bursting of the photon stop, safety measures were enforced, such as an automatic closure of all helium valves in the case of loss of water flow or the safety heaters, and additional safety measures provided, such as installation of a manual compressed air line to blow out water from the stop. Other limitations appeared in the cryo-system. For example, the liquid helium transfer line between the refrigerator and the photon-stop was inadequately designed and did not permit transfer of liquid. Therefore the dummy cold mass circuit could not be operated at the temperature lower than ~15 K. Furthermore, the refrigerator could not be operated at the specified liquid helium production rate and was often used in the batch mode.

The experiment, however, was concluded successfully with a flawless, continuous operation over 4 weeks. All circuits operated more or less as expected and therefore the major goal of this experiment was achieved. The measurement of the residual heat load on the various sub-systems, which was a secondary purpose of the experiment, was also conducted. The long-term goal for the residual heat load on the cold mass system per photon stop is < 1 W in order for the photon stop system to be a competitive solution for a future hadron collider. This goal was not achieved in this experiment. It is, however, not entirely clear following this experiment, whether the additional heat load in the system was inherent to the design or the result of spurious heat loads that were present in the system. These spurious or accidental heat loads were 1) radiation from the water tubes leading to the photon stop, which had not been shielded with MLI and 2) radiation from ambient due to the insufficient cooling of the cryostat thermal shield (and in particular the end-caps). Model calculations indicate that in fact the design goals would have been achieved without presence of these accidental heat sources.

Summarizing, it has to be noted that one of the most important aspects of this experiment was a valuable learning experience that will allow considerable improvement to the design and test procedures for the next generation of photon stop prototypes.

REFERENCES

[1]   P. Limon et al., "*Design Study for a Staged Very Large Hadron Collider*", Fermilab-TM-2149, June 2001

[2]   C. Darve et al: "*VLHC beam-screen cooling*", Fermilab, Technical Division Note TD-01-005, Feb. 2001

[3]   P. Bauer et al., "*Synchrotron Radiation Issues in the VLHC*", Proceedings to the Particle Accelerator Conference 2001, Chicago, Sept. 2001

[4]   P. Bauer et al., "Synchrotron Radiation Absorbers for Hadron Colliders", Proceedings of the European Particle Accelerator Conference, Paris, France, June 2002

[5]   P. Bauer et al. "*A Photon Stop for the VLHC-2, Engineering Design I*", Fermilab, Technical Division note, TD-01-023, April 2001

APPENDIX A – ADDITIONAL PICTURES

Figure 24: Some of the participants in the photon stop cryo-test.

Figure 25: During the photon stop test in Fermilab's Meson cryolab.

APPENDIX B – HEATERS

Table 9 lists all heaters used in the photon stop cryo-test and describes their function. These heaters were all of the flexible foil type and surface mounted with epoxy. They use a special Ni-Cr steel alloy as resistive materials, which is characterized by little change in resistivity from room to cryogenic temperature.

Table 9: Name and purpose of heaters used in the photon stop cryo-test.

ACCNET	#	location	purpose
YPSTOP	YP01	photon stop top	safety heater 1
YPSBOT	YP02	photon stop bottom	safety heater 2
YPSNO1	YP03	photon stop nose (in series with YPSNO2)	simulates synchrotron radiation heating on PS tip
YPSNO2	YP04	photon stop nose (in series with YPSNO1)	simulates synchrotron radiation heating on PS tip
YPTS	YP05	photon stop thermal shield	heater for Q0 measurement
YTS	YP06	cryostat thermal shield	heater for Q0 measurement
YBS	YP07	beam screen	heater for Q0 measurement
YCM	YP08	cold mass	heater for Q0 measurement

The resistance of the various heaters was measured at room temperature and at ~85 K (in liquid nitrogen bath). As expected, the measured resistance change is small (<1 %). Therefore in the data analysis the heater resistance was assumed to be the room temperature value. Figure 26 shows an example of the heaters used.

Figure 26: Minco heaters

APPENDIX C – FLOWMETER CALIBRATION

I. 5 K helium flow was measured with an Omega™ turbine flowmeter model SP01 ¼-CB-PH15-B-4RFX attached to FTB-937 turbine housing of 29.65 mm ID. The flowmeter was calibrated by OMEGA as Freq [Hz] vs. Flow [acfm He]. Additional freq-to-voltage converter is added to produce 0-5V output to the control system. Assuming that 0-1000 Hz is linear to 0-5V DC, then the calibration data and curve are shown in Table 10 and Figure 27.

Table 10: Omega SP01 ¼-CB-PH15-B-4RFX calibration data.

Freq, Hz	ACFM He	T,F	P,psia	Ro, kg/m3	Flow, g/s
420.2	17.50	82.983	16.716	0.18395	1.519
479.8	19.84	83.045	16.683	0.18356	1.719
565.7	23.23	83.078	16.697	0.18371	2.014
681.1	27.78	83.062	16.717	0.18393	2.411
800.0	32.48	82.446	16.691	0.18385	2.818
899.3	36.47	82.732	16.701	0.18387	3.165
1025.5	41.60	82.762	16.791	0.18485	3.629
1163.2	47.18	82.734	16.682	0.18366	4.090
1309.5	53.13	82.45	16.684	0.18377	4.608
1531.0	62.18	81.497	16.802	0.18540	5.441
1750.0	71.14	82.512	16.742	0.18439	6.191
1950.0	79.48	82.117	16.849	0.18571	6.966
2322.0	94.84	82.361	16.796	0.18504	8.282

Please note that the calibration data is for volumetric flow above 17.5 acfm He, or 1.52 g/s at 82^oF and 16.7 psia. Therefore, a typical 1 g/s of 5 K helium flow was below the certified calibration range. To verify the flow measurements, we made a special test with precise flow rotameters. These experiments (see data in Figure 28) showed that the friction in the turbine flowmeter becomes an overwhelming factor at low flow rates, and the turbine stops spinning at ~ 4.5 acfm He, which is ~ 0.4 g/s of helium at 82^oF and 16.7 psia. Therefore, we conclude that though the 5^oK flow measurements were reasonably accurate above 0.4 g/s, experiments at flows below 0.4 g/s suffered from irregular flow due to friction effects on the turbine. These effects are believed to be the reason for large (±50%) fluctuations in the flow data in cases with 0.3 g/s flow.
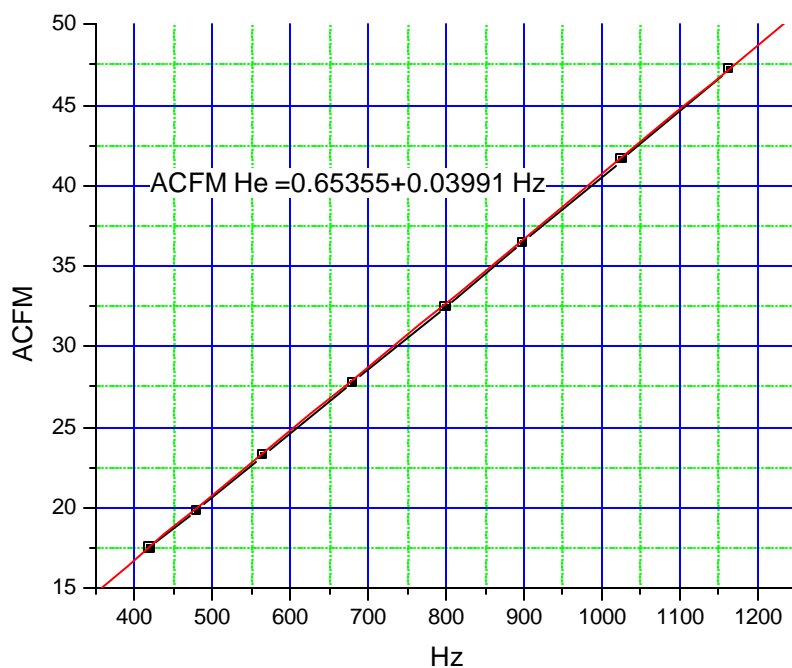
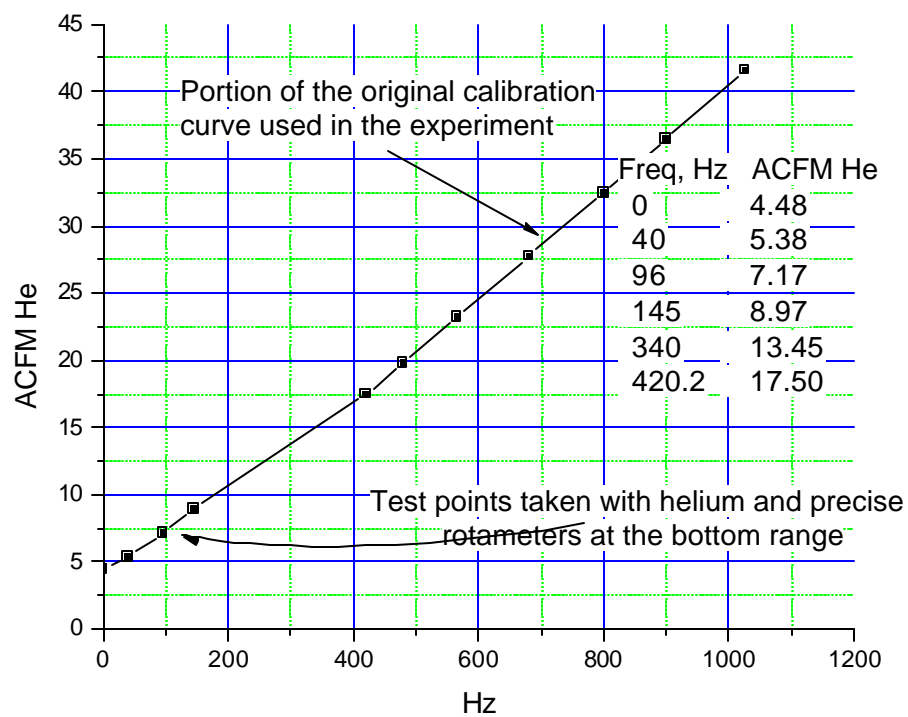Figure 27: Omega SP01 ¼-CB-PH15-B-4RFX calibration plot.

Figure 28: Calibration of Omega SP01 ¼-CB-PH15-B-4RFX flowmeter for small flow.

II. 30 K helium flow was measured with Aeroquip Barco™ venturi 1-1/4"- 588 with the following Flow [gpm] vs. ?P [psi] relationship (see Figure 29):

$$GPM = 0.75649 + 1.96398\,?P\text{-}0.1208\,?P^2 + 0.00426\,?P^3 - 6.9277610^{-5}\,?P^4 + 4.154510^{-7}\,?P^5$$

Using equation for venturi $Flow_{He}, cfm = \dfrac{3.8}{\sqrt{0.138141}}\sqrt{\dfrac{14.7 + P_{He}}{14.7}}\sqrt{\dfrac{530}{T_{He} + 460}} \cdot GPM \cdot r_{He}$ and

general flow conversions: $schmAir = 3.8 \cdot gpmH2O$ and $1g/s_{He} = 4.4 scfmAir$, we then use

the following fit to calculate the flow: $Flow_{He}, g/s = 5.2395 \cdot \sqrt{\dfrac{14.7 + Ppsig}{T,F + 460}} \cdot GPM$.

For 1.5 psig 70°F inlet conditions, the helium mass flow through the venturi is shown in Figure 30. It is again obvious that the measurements were conducted at the bottom range of the calibration curve.
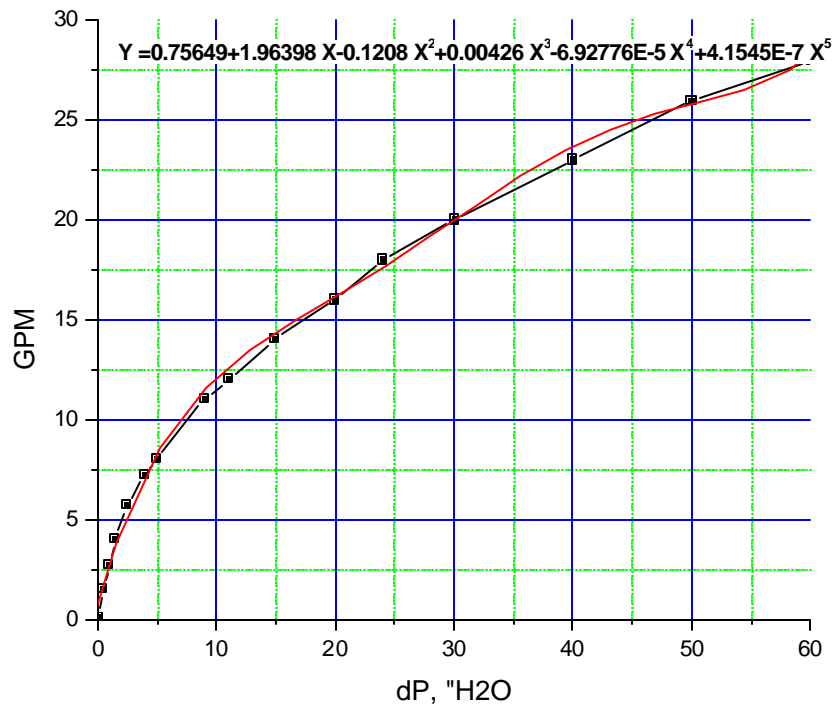

Figure 29: Aeroquip Barco™ venturi flowmeter calibration for helium gas in gpm.
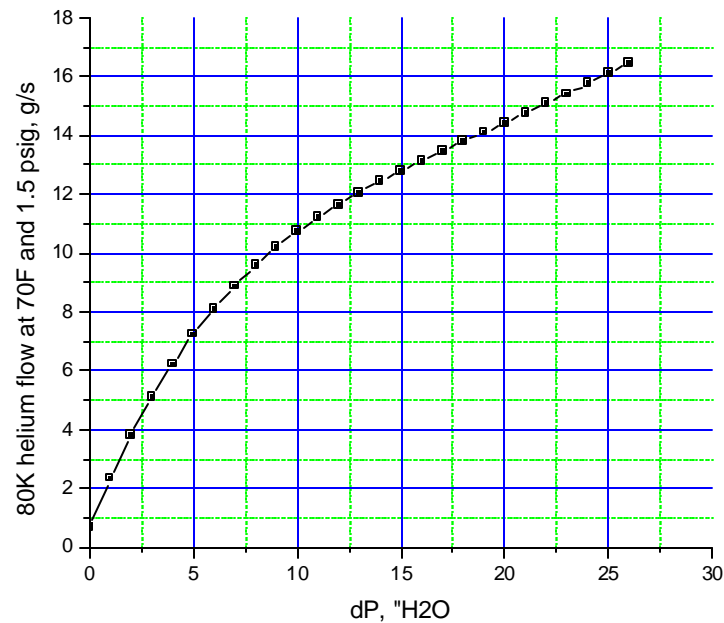
Figure 30: Aeroquip Barco™ venturi flowmeter calibration in effective 80 K helium gas flow.

III. Water flow was measured with Aeroquip Barco™ venturi 1"- 567 with the following Flow [gpm] vs. ?P [psi] relationship (see Figure 31):

$$GPM = 0.19565 + 1.17692?P - 0.07856?P^2 + 0.00297?P^3 - 5.1882410^{-5} ? P^4 + 3.3489610^{-7} ? P^5$$

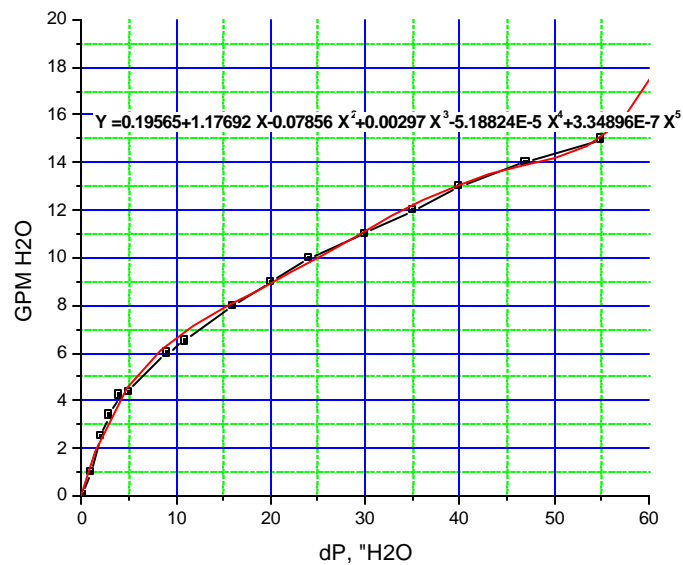The range of measurements was [0.3-1.0] liter/s, or [4.74-15.8] gpm.

Figure 31: Aeroquip Barco™ venturi 1"- 567 calibration for the water flow measurement.

APPENDIX D – TEMPERATURE MEASUREMENT

Temperature sensors

The temperature measurements for the photon-stop cryotest were performed using Cernox[TM] (CX-1050-SD) and Platinum (PT102) type sensors, trademark of LakeShore's. The temperature sensors were read out with the four-wire measurement technique to minimize the influence of the wire resistance. In the case of the Cernox sensors the current was controlled by a LakeShore Model 234 D temperature transmitter to maintain a constant voltage and limit the self-heating. Each of the existing four Cernox sensors was calibrated by Lakeshore in the temperature range of 4.2 K to 325 K and the data were fitted with 6th order Chebychev polynomials for multiple, narrow temperature ranges. The PT102 temperature sensor is LakeShore model PT102 made of platinum with a temperature range of operation between 30 and 300 K. The resistance stability of both ceramic oxide and platinum materials should allow for repeatable and reliable measurement in their relative operating temperature range even after repeated thermal cycling. The sensitivity of the CX-1050-SD and PT102 are on order of 10^{-3} Ω/K at 5 K and 0.4 Ω/K at 70 K, respectively.

Estimate of possible measurement errors

The following paragraphs list the various sources of possible temperature measurement errors in the case of the Cernox sensors. These two factors are reported in a separated section.

The error in the Chebychev fit is +/-10 mK for temperatures lower than 10 K (and +/- 20 mK at 20 K) for the Cernox sensors according to the LakeShore sensor specification sheet). This error can easily be doubled when using simpler fits (such as the polynomial fit used in some instances in the photon stop cryotest analysis).

LakeShore also claims to measure the temperature with 4 mK resolution during the calibration measurement.

The temperature uncertainty related to an uncertainty in voltage measurements can be estimated with:

$$\frac{u_T}{T} = \frac{u_v/V}{(T/V)(dV/dT)} \equiv \frac{u_v/V}{S_T} \ , \tag{B1}$$

where u_V is the voltage uncertainty and S_T, is the dimensionless temperature sensitivity, defined as $S_T = (T/V)(dV/dT)$. The condition where the cold mass temperature is 10 K is considered. The LakeShore temperature monitor Model 234D has a specified DC voltage accuracy of $u_{Vlin}/V = 0.04\%$ and performs the sensor reading at a fixed voltage of ~30 mV. The dimensionless sensitivity is given as $S_T = 1.2$. Assuming an additional, typical voltage uncertainty of $u_{voff} = 3.5$ μV and an additional noise voltage $u_{noise} = 1$ μV the following error-estimates can be made on the basis of (B1):

$$u_{Vread} = \left(\frac{T}{S_T}\right)\left(\frac{U_{Vread}}{V}\right) = \left(\frac{10K}{1.2}\right)\left(4 \cdot 10^{-4}\right) = 3.3 \text{ mK} \tag{B1a}$$

$$u_{Voff} = \left(\frac{T}{S_T}\right)\left(\frac{U_{Voff}}{V}\right) = \left(\frac{10K}{1.2}\right)\left(\frac{0.0035 mV}{30 mV}\right) = 0.97 \text{ mK} \tag{B1b}$$

$$u_{Vnoise} = \left(\frac{T}{S_T}\right)\left(\frac{U_{noisei}}{V}\right) = \left(\frac{10K}{1.2}\right)\left(\frac{0.001 mV}{30 mV}\right) = 0.3 \text{ mK} \tag{B1c}$$

The stability of the current in the LakeShore 234D temperature transmitter is specified to be stable to within ±5 µA, therefore an entirely negligible contribution to the measurement error.

The temperature rise due to the self-heating, DT_{sh}, depends on the excitation current and is governed by

$$\Delta T_{sh} = P_s \cdot R_t = I^2 R_e R_t = P_{sopt} R_t \ , \tag{B2}$$

where R_t and R_e are the thermal resistance between the sensor and its environment and the electrical resistance, respectively and P_{sopt} is the (optimized) electrical heating in the sensor during measurement. According to LakeShore the sensor electrical resistance at 10 K is R_e = 1375 Ω, the dimensionless sensitivity S_T = 1.2 and the thermal resistance R_t = 1070 K/W. The sensor heating power therefore is

$$P_{sopt} = \left(\frac{T^2}{2R_e S_T^2 R_t^2}\sum (u_{Vi})^2\right)^{1/3} = \left\{\frac{(10K)^2}{(2 \cdot (1375\,\Omega)(1.2)^2(1070\,K/W)^2)}\left[(3.5 \cdot 10^{-6}V)^2 + (1 \cdot 10^{-6}V)^2\right]\right\}^{1/3}$$

$$P_{sopt} = 664 \text{ nW} \tag{B3}$$

The temperature rise in the sensor due to self-heating as obtained from B2 and B3 then becomes:

$$U_{tsh} = \Delta T_{sh} = P_{sopt}\ R_t = 664\ 10^{-9}\ W\ .\ 1070\ K/W = 0.7\ \text{mK}$$

Summing the above, one obtains:

$$U_T = \sqrt{\sum_i (u_i^2)} \ \sim 20 \text{ mK}$$

A similar calculation could not be performed for the Pt sensors because the parameters are less known. The reading of the PT102 sensor was performed by the APACS systems using 50 μs long pulsed currents of 2.5 mA. The error for the excitation current is of the order of 0.1 %. If a similar uncertainty is assumed for the temperature readings, the uncertainty on the ~50 K temperatures would be 50 mK.

The Cernox sensors were attached to the cold mass by means of a thin layer of Stycast (epoxy type). The Cernox are surrounded by vacuum. Platinum resistors were also mounted with Stycast to the cooling tubes. After the "incident" of the frozen photon stop tip, PT102 sensors and their Stycast layer were detached from the cooling tube. Hence resin VGE-7031 was used to reattach the PT102 sensors to the tubes. The temperature response times appeared to be of the order of 20 ms at 10 K and 100 ms at 77K, indicating a good thermal contact between the sensor and the cooling tubes. The temperature measurement error introduced by the thermal impedance between the sensor and the to be measured object is difficult to quantify.

Temperature data were transferred to ACNET from the APACS system. The measured voltages were amplified by a gain of 40 (programmable gain instrumentation amplifier) and digitized by a 12 (9??) bit, self-calibrated A/D converter and stored in the computer module memories. Its accuracy should therefore be sufficient, of the order of 0.024 %. As for the PT102 temperature sensor, the error for the excitation current is of the order of 0.1 %. This resolution depends on the Meson I/O rate. The conditioning used in the APACS I/O, represents a major source of error and is difficult to quantify.

The measurement of the CX-1050-SD was possible by using the temperature transmitter 234-D, which transmitted a 0-5 Volt signal to the APACS I/O. The read-out was then accessible through ACNET with a similar procedure to the one described for the PT102.

Case analysis

A full set of measurements required at least 2 hours of data acquisition. The stabilization period after powering one of the heaters lasted between 10 and 20 minutes. Temperature differences between the beginning and the end of a measurement period are usually less than 1.2 K for the warm helium circuit and less than 100 mK for the cold helium circuit. The temperature fluctuations during a measurement were studied for case H (Table 3), in which the warm helium and cold helium loops were at ~50 K and ~25 K, respectively. The photon stop temperature was 271 K. The temperature fluctuations can be see in the plots shown in Figure 15 and Figure 16.

Table 1 summarizes the standard deviation for both circuits. For the Cernox temperature sensors (cold helium loop) the deviation is smaller than 200 mK. The standard deviations are listed in table 2 for the temperature on the warm helium circuit. Larger fluctuations are observed for Platinum temperature sensors than for the Cernox. Up to 1.2 K of difference can be measured.

Table 11: Temperature variation in cold and warm helium circuit over 20 min (case H).

sensor variation (K)	TCMIN	TCMMI	TCM3	TCMOU		flow FTM1	
	0.144	0.206	0.087	0.120		0.004	
sensor variation (K)	TCPTSI	TCPTSO	TCTSIN	TCTSOU	TCBSIN	TCBSOU	flow FTM2
	0.14	0.14	0.11	0.07	0.22	0.17	0.01

The temperature fluctuations quoted in Table 11 are ~10 times larger than expected.

**Process parameter variations**

The expected error in the temperature measurements as outlined above is much smaller than the observed temperature fluctuations. These fluctuations are believed to be mostly the result of process variable variations, such as variations in the flow.

The effect of spurious heating on the temperature reading

See detailed discussion in paragraph 3.5 of the report.

Conclusions

The observed temperature variations were sufficiently small and most likely the result of process parameter variations, such as flow variations. More important, however, was the effect of direct heating of the sensors by radiation from the unshielded water tubes (as well as from the insufficiently cooled cryostat thermal shield). Also mounting techniques were not reliable.

APPENDIX E – SAFETY REVIEW

Fermilab
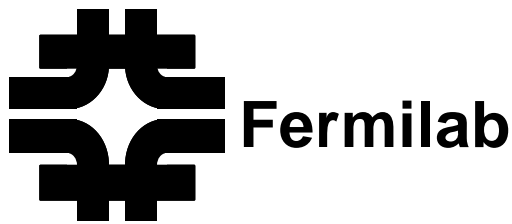
21 November 2002

To: John Anderson, BD/ES&H
Cc: Rich Schmitt, Cryogenic Safety Committee Chair

From   Meson Cryo Review sub-Panel: Joel Misek, Michael Geynisman, Alex Martinez, and Dave Pushka

Subject: Walk-thru and peer review of theVLHC2 Photon Stop Experiment in Meson Cryo Test Facility

BACKGROUND INFORMATION:

A photon stop mock-up apparatus has been designed and will be tested in Meson Cryo for the purpose of verifying the thermal model of the proposed VLHC2 photon stop cryogenic design. This test set-up will determine if a small water-cooled metal block in the cold volume (meant to absorb photon energy from a VLHC beam) is feasible.

This system is being assembled by Michael Geynisman and draws on existing infrastructure provided by Alex Martinez. Therefore, 50% of the small sub-committee is directly involved in the execution of this work.

Future short duration experiments are planned for the Meson Cryo Test Facility. One may reasonably conclude that the level of documentation and review conducted on the VLHC2 Photon Stop Experiment will set a precedent for future projects.

FINDINGS:

TheVLHC2 Photon Stop Experiment uses helium from one of the three refrigerators in the Meson Cryo Test Facility. Meson Cryo is currently classified as ODH 0. The ODH classification does not change for this building based on the argument that only one of three refrigerators will run and the number of potential failure points added by the VLHC2 Photon Stop Experiment equipment is small compared to the number of points from the two idle refrigerators.

Meson Cryo Test Facility has recently been reviewed and has operated for several weeks, including un-attended nights.

During the operation of the Photon Stop Experiment, the brown refrigerator in Meson Cryo will operate 24 hours a day, but the experiment will only be operated while staffed.

The Piping and Instrumentation Diagram (P&ID) for the VLHC2 Photon Stop Experiment has been sketched on to a copy of the existing Flow Schematic for the Meson Cryo Test Facility.

An Engineering Analysis Note was generated to explain the safety aspects of the installation and of operations for the VLHC2 Photon Stop Experiment.

Neither instrument lists nor What-If analysis has been generated.

Two vacuum insulated vessels have been used in this test set-up. The combined evacuated volume is less than that which would require an engineering note per FESHM 5033.

A "BR" valve box with a completed silver sticker is used in the test set-up.

Data logging and control of the test set-up will be via ACNET.

There are no pressure vessels internal to the experimental set-up vacuum insulation vessel. All liquid and gas lines in this vessel are small diameter copper and stainless tubes using Swagelok VCR connections.

Heaters are installed in the experimental set-up vacuum insulation vessel and are powered with a variety of commercial power supplies. Fuses will be added to limit the current in the heaters and the wiring to the heaters to levels consistent with the rating of the heaters and wiring.

Michael Geynisman will consider a means by which to blow water out of the small water-cooled metal block in the cold volume in the event of a heater failure. This is not a safety issue, rather an operational issue to limit damage due to water freezing (and causing damage to the test set up) in the event of a power failure.

The area immediately around the VLHC2 Photon Stop Experiment will be cordoned off during running of the experiment.

Running of this test set up is planned to take only three weeks time and should conclude before January 2003. After the conclusion of the test, the equipment will be disassembled.

RECOMMENDATIONS:

None. The purpose of this walk-thru was to provide a peer review of the system by people not directly involved in the assembly of the system. This has been accomplished. No obvious deficiencies or conditions that would result in either equipment damage or present a personal safety hazard were found.

APPENDIX F – PURCHASE SUMMARY

Drawing/Part No.	Description	Qty.	Rec'vd.	Act. Cost	Order #	Vendor
CX-1050-SD	Cernox Sensor(uncalibrated)	6	7/19/2002	$966.00	PRN23541	Lake Shore
	Cernox Sensor Calibration	6		$2,077.00	PRN24596	Lake Shore
PT-102	Platinum Sensor(uncalibrated)	10	7/19/2002	$634.80	PRN23541	Lake Shore
ES-2-20	Stycast epoxy 20/2 gram packs	4	7/19/2002	$684.00	PRN23541	Lake Shore
8-8 QHW-SSR	Parker connector	4	7/15/2002	$54.96	PRN23549	Inst. Assoc.
8-8 Q1W-SSW	Parker connector	4	7/19/2002	$50.44	PRN23549	Inst. Assoc.
8-QO-SS	O-ring	4	7/19/2002	$10.04	PRN23549	Inst. Assoc.
IS1600600BB	Flange, bored blankoff	2	7/16/2002	$150.00	PRN23555	Varian
IC160250A	Clamp, double jaw	10	7/16/2002	$45.00	PRN23555	Varian
FTB-937	Gas turbine flowmeter w/ calibration	1		$1,669.00	PRN24156	Omega
SS-4-VCO-61	VCO bulkhead	1	7/12/2002	$23.48	PRN23578	Fluid Systems
SS-4-VCO-3	VCO gland	2	7/12/2002	$8.36	PRN23578	Fluid Systems
SS-4-VCO-1	VCO coupling	2	7/12/2002	$16.88	PRN23578	Fluid Systems
SS-4-VCO-4	VCO nut	2	7/12/2002	$9.68	PRN23578	Fluid Systems
SS-4-VCR-61	VCR bulkhead body	1	7/12/2002	$21.20	PRN23578	Fluid Systems
SS-4-VCR-3	VCR gland	12	7/12/2002	$79.20	PRN23578	Fluid Systems
SS-4-VCR-1	VCR female nut	6	7/12/2002	$25.80	PRN23578	Fluid Systems
SS-4-VCR-4	VCR male nut	6	7/12/2002	$21.60	PRN23578	Fluid Systems
SS-8-VCO-61	VCO bulhead union	6	7/26/2002	$194.40	PRN23578	Fluid Systems
SS-8-VCO-3	VCO gland	12	7/12/2002	$84.36	PRN23578	Fluid Systems
SS-8-VCO-1	VCO coupling	6	7/12/2002	$80.94	PRN23578	Fluid Systems
SS-8-VCO-4	VCO nut	6	7/12/2002	$49.50	PRN23578	Fluid Systems
SS-T8-035-20	SS tubing 1/2"OD x .035"wall	20FT	7/12/2002	$82.00	PRN23578	Fluid Systems
OAL TLWB316L	C/W rotateable flange 1.5"ID x 6.37"	1	8/2/2002	$150.00	PRN23579	American BOA
OAL TLWB316L	C/W rotateable flange 3"ID x 7.5"	1	8/2/2002	$270.00	PRN23579	American BOA
8667K213	G-10 1/8 x 12 x12	1	7/12/2002	$12.66	PRN23593	McMaster
8667K35	G-10 1/4 x 36 x 48	1	7/12/2002	$165.94	PRN23593	McMaster
8667K277	G-10 3/8 x 24 x 24	1	7/12/2002	$106.83	PRN23593	McMaster
8967K35	Copper tubing 1.25"OD x .065	6FT	7/17/2002	$51.94	PRN23866	McMaster
8967K14	Copper tubing 1.5"OD x .032	6FT	7/17/2002	$34.64	PRN23866	McMaster
8963K76	Copper sheet .032 x 36 x 48	1	7/17/2002	$74.00	PRN23866	McMaster
KHLV-105/10	Kapton heater	5	7/30/2002	$120.95	PRN23869	Omega
6313-14-19P-SP-M134	Electrical connector, 19 pin gold pltd	10	7/29/2002	$750.00	PRN23945	BTC
	Copper tubing C101 3"OD x .125	6FT	8/2/2002	$298.00	546324	McCaffrey
HK5574R4.6L12D	Heater	2	7/30/2002	$$48.30	PRN24163	Minco
4-BQ-SS	Size 4 Ultraseal nuts	2	8/13/2002	$12.78	PRN24522	Inst. Assoc.
4-4 Q1T3-SSR	Ultraseal gland to size 4 Male tube	2	8/13/2002	$55.44	PRN24522	Inst. Assoc.
4-QO-SS	Kel-F O-ring	5	8/13/2002	$14.80	PRN24522	Inst. Assoc.
4-4 Q1RT3-SSR.035	Size 4 Ultraseal inverted gland to 4	2	8/13/2002	$42.86	PRN24522	Inst. Assoc.
4-BQI-SS	Size 4 Ultraseal Male weld nut	2	8/13/2002	$10.88	PRN24522	Inst. Assoc.
				$9,258.66		

APPENDIX G – THERMAL MODEL CALCULATIONS

Photon stop cryo-test thermal design - Based on case B
Ch. Darve / P. Bauer   02/16/03

1. NOMENCLATURE

Notations:

t: temps

T: temperature

PS: Photon stop   : Copper
TSPS: Photon stop thermal shield   : Copper
BS: Beam screen   : Copper
CM: Cold Mass   : Copper
MLI: Multi-Layer-Insulation   : Mylar polyester film and spacers
TS: Cryostat Thermal Shield   : Aluminum
VV: Vacuum Vessel   : Stainless Steel

2. DATA

2.1 Temperatures:

$Tvv := 300 K$:Temperature of the vacuum vessel

$Tpstsin := 78 K$ $Tpstsout := 79 \cdot K$

$Tpsts := \dfrac{(Tpstsin + Tpstsout)}{2}$: Temperature of the photon stop thermal shield $Tpsts = 78.5 K$

$Ttsin := Tpstsout$ $Ttsout := 80 \cdot K$

$TcryostatTS := \dfrac{(Ttsout + Ttsin)}{2}$: Cryostat Thermal shield temperature $TcryostatTS = 79.5 K$

$Tbsin := Ttsout$ $Tbsout := 81 \cdot K$

$Tbs := \dfrac{(Tbsout + Tbsin)}{2}$: Temperature of the beam screen $Tbs = 80.5 K$

$Tpsin := 270 K$ $Tpsout := 276 K$

$Tps := \dfrac{(Tpsout + Tpsin)}{2}$: Temperature of the photon stop $Tps = 273 K$

$Tcm := 19 \cdot K$: Temperature of the cold mass $Tcm = 19 K$

$Tend := TcryostatTS + 20 \cdot K$: Temperature of the end cap $Tend = 99.5 K$

$Twater := 285 K$: Temperature of the water $Twater = 285 K$

2.2 Constants:

$PV := 10^{-6}$ [mbar]   : Vacuum

$\sigma := 5.67 \cdot 10^{-8} \dfrac{watt}{m^2 \cdot K^4}$: Stefan-Boltzmann's constant

2.3 Dimensions

Lengths   **Diameters**   **Surfaces**

$Lvv := 69 \cdot in$ $Lvv = 1.753 m$ $Dvv := 10.2 \cdot in$ $Dvv = 0.508 m$ $Svv := \pi \cdot (Dvv) \cdot Lvv$ $Svv = 2.797 m^2$

$Lbs := 60 \cdot in$ $Lbs = 1.524 m$ $Dbs := 1.5 \cdot in$ $Dbs = 0.038 m$ $Sbs := \pi \cdot Dbs \cdot Lbs$ $Sbs = 0.182 m^2$

$Lcm := 52 \cdot in$ $Lcm = 1.321 m$ $Dcm := 3 \cdot in$ $Dcm = 0.076 m$ $Scm := \pi \cdot Dcm \cdot Lcm$ $Scm = 0.316 m^2$

$Lct := 463.143 \cdot in$ $Lct = 11.006 m$ $Dct := 0.25 \cdot in$ $Sct := \pi \cdot Dct \cdot Lct$ $Sct = 0.22 m^2$

$Ltsbellow := 28 \cdot in$ $Dtsbellows := 3 \cdot in$ $Stsbellows := \pi \cdot Dtsbellows \cdot Ltsbellow$ $Stsbellows = 0.17 m^2$

    $Ltsbellow = 0.711 m$ $Dts := Dvv$

$Lps := 19.75 in$ $Lps = 0.502 m$ $Dps := 34.8 mm$ $Sps := \pi \cdot Dps \cdot Lps$ $Sps = 0.055 m^2$

$Lpstsbellows := 24 \cdot in$ $Dpstsbellows := 1.5 \cdot in$ $Spstsbellows := \pi \cdot Dpstsbellows \cdot Lpst$ $Spstsbellows = 0.073 m^2$

$Lpsts := 12 \cdot in$ $Dpsts := 2 \cdot 0.755 in$ $Spsts := \pi \cdot Dpsts \cdot Lpsts$ $Spsts = 0.037 m^2$

A. Vacuum Vessel to Cryostat Thermal shield

$DcryostatTS := 9.6372 \cdot in$: Thermal shield diameter $DcryostatTS = 0.49 m$

$LcryostatTS := 60 \cdot in$: Thermal shield length $LcryostatTS = 1.524 m$

$Surf\_cryostatTS := LcryostatTS \pi \cdot DcryostatTS$: Thermal shield surface $Surf\_cryostatTS = 2.344 m^2$

$DcryostatVV := Dvv$: Vacuum vessel diameter

$LcryostatVV := Lvv$: Vacuum vessel length

$Surf\_cryostatVV := LcryostatVV \pi \cdot DcryostatVV$: Vacuum vessel surface $Surf\_cryostatVV = 2.797 m^2$

$Lspider := 4.5 \cdot in$ $Lspider = 0.114 m$: Spider thermal length

$Aspider := 8 \cdot 1 \cdot in \cdot 0.25 in$: Spider surface (x 8 blocks) $Aspider = 1290.32 mm^2$

B. Beam screen to cold mass

$wbs\_cm := 0.12 \cdot in$: Beam screen - cold mass - azi. contact area $wbs\_cm = 3.048 mm$

$contactbs\_cm := 60 \cdot deg \cdot \dfrac{2.925 in}{2}$: Beam screen - cold mass - wide $contactbs\_cm = 38.901 mm$

$Abs\_cm := 3 \cdot 2 \cdot contactbs\_cm \cdot wbs\_cm$: Beam screen to CM transfer area (x2 spider . x3 contacts)) $Abs\_cm = 7.114 \cdot 10^{-4} \cdot m^2$

$Dcmi := Dcm - 2 \cdot 0.125 in$: Inner diameter cold mass

$Lbs\_cm := \dfrac{(Dcmi - Dbs)}{2}$: Thermal length $Lbs\_cm = 0.625 in$

C. Cryostat Thermal Shield to beam screen - large spider - end cap

$wts\_bs := 0.25 in$ $wts\_bs = 6.35 mm$: Cryostat Thermal shield - Beam screen - wide $wts\_bs = 0.006 m$

$Ats\_bs := 2 \cdot 3 \cdot 0.62 in \cdot wts\_bs$: Cryostat Thermal shield - Beam screen - transfer area $Ats\_bs = 599.999 mm^2$
                                         (x3 contact , x2 spider)

$Lts\_bs := 60 \cdot deg \cdot 14.75 in$: Cryostat Thermal shield - Beam screen - thermal length $Lts\_bs = 0.392 m$

$Lts\_bs = 0.392 m$ 60 degree x Radius spider

$Sendcap := 2 \cdot 3.14 \cdot \dfrac{Dts^2}{4}$: Surface of the end cap (x2) $Sendcap = 0.405 m^2$

D. Beam screen to photon stop - G10 pins

$Dbs\_ps := 0.25 in$: Diameter of the G10 pin $Dbs\_ps = 6.35 mm$

$Lbs\_ps := \dfrac{Dbs\_ps}{2}$: Beam screen - photon stop - thermal length $Lbs\_ps = 3.175 mm$

$Abs\_ps := \dfrac{3 \pi \cdot Dbs\_ps^2}{4}$: Beam screen - photon stop - transfer area (x3 sphres) $Abs\_ps = 95.008 mm^2$

$Aps\_psts := Abs\_ps$: Notation

E. Bellows

$Dtsbellows = 3 \cdot in$: Diameter tsbellows - outer bellows $Dtsbellows = 0.076 m$

$Tck\_ts := 0.15 mm$: Thickness tsbellows

$Dtsi := Dtsbellows - 2 \cdot Tck\_ts$: Inner diameter tsbellows $Dtsi = 2.988 in$

$Ats\_bellows := \pi \cdot \dfrac{\left(Dtsbellows^2 - Dtsi^2\right)}{4}$: Transfer area tsbellows $Ats\_bellows = 35.838 mm^2$

$Dpsts = 1.51 \cdot in$

$Tck\_psts := 0.15 mm$: Thickness pstsbellows - inner bellows

$Dpstsi := Dpstsbellows - 2 \cdot Tck\_ts$: Inner diameter pstsbellows $Dpstsi = 1.488 \cdot in$

$Apsts\_bellows := \pi \cdot \dfrac{\left(Dpsts^2 - Dpstsi^2\right)}{4}$: Transfer area pstsbellows $Apsts\_bellows = 33.135 mm^2$

F. Water pipes   Water line size = 0.5 in dia* 50 cm long * 2 tubes

$diawaterpipe := 0.5 \cdot in$: Water tube diameter $diawaterpipe = 0.013 m$

$Lwater := 50 \cdot cm$: Water tube length

$Swaterpipe := diawaterpipe \cdot 3.14 Lwater \cdot 2$: Water pipe surface (x2 pipes) $Swaterpipe = 0.04 m^2$

G. Photon stop thermal shield

$Apsts\_wall := 3.14 \cdot \dfrac{\left[(1.5 \cdot in)^2 - (1.45 \cdot in)^2\right]}{4}$: Cross-section of the photon stop thermal shield $Apsts\_wall = 7.47 \cdot 10^{-5} \cdot m^2$

2.4 Material Properties

A. Conductivity

$$Temp := \begin{bmatrix} 1.8 \\ 3 \\ 5 \\ 7 \\ 10 \\ 20 \\ 30 \\ 50 \\ 100 \\ 200 \\ 293 \end{bmatrix} \cdot K \qquad G10 := \begin{bmatrix} .035 \\ .059 \\ .090 \\ .120 \\ .150 \\ .190 \\ .24 \\ .29 \\ .43 \\ .65 \\ .8 \end{bmatrix} \frac{watt}{m \cdot K}$$

$$kG10(T) := linterp(Temp, G10, T)$$

$$TCu := \begin{bmatrix} 4 \\ 6 \\ 8 \\ 10 \\ 20 \\ 25 \\ 30 \\ 35 \\ 40 \\ 50 \\ 60 \\ 70 \\ 80 \\ 100 \\ 150 \\ 200 \\ 300 \end{bmatrix} \cdot K \qquad Cu := \begin{bmatrix} 320 \\ 450 \\ 650 \\ 800 \\ 1300 \\ 1400 \\ 1350 \\ 1300 \\ 1180 \\ 850 \\ 680 \\ 580 \\ 530 \\ 450 \\ 420 \\ 384 \\ 384 \end{bmatrix} \frac{watt}{K \cdot m}$$

$$kCu(T) := linterp(TCu, Cu, T)$$

$$Tss := \begin{bmatrix} 4 \\ 6 \\ 8 \\ 10 \\ 15 \\ 20 \\ 25 \\ 30 \\ 35 \\ 40 \\ 50 \\ 60 \\ 70 \\ 80 \\ 90 \\ 100 \\ 120 \\ 140 \\ 160 \\ 180 \\ 200 \\ 250 \\ 300 \end{bmatrix} \cdot K \qquad SS := \begin{bmatrix} 0.24 \\ 0.39 \\ 0.57 \\ 0.77 \\ 1.32 \\ 1.95 \\ 2.6 \\ 3.3 \\ 4.0 \\ 4.7 \\ 5.8 \\ 6.8 \\ 7.6 \\ 8.3 \\ 9.0 \\ 9.5 \\ 10.3 \\ 11.0 \\ 12.0 \\ 12.3 \\ 13.0 \\ 14.0 \\ 15.0 \end{bmatrix} \frac{watt}{K \cdot m}$$

$$kSS(T) := linterp(Tss, SS, T)$$

B. Specific Heat of supercritical He at 2 bar - Data from HEPAK

Y := READPRN("He_35psia.prn")

$$Temp := Y^{<1>} \cdot K$$

$$cpHe := Y^{<5>} \frac{joule}{kg \cdot K}$$

$$cpHe(T) := linterp(Temp, cpHe, T)$$

$$T := 4 .. 100$$

$$HHe := Y^{<6>} \frac{joule}{kg}$$

$$HHe(T) := linterp(Temp, HHe, T)$$

$$cpHe(4.6 K) = 5427 \, kg^{-1} \bullet K^{-1} \bullet joule$$

$T := 0 \cdot K .. 300 \cdot K$

<div style="display:flex">

| density | viscosity | conductivity | specific heat | enthalphy |
</div>

$$\rho He := Y^{<2>} \frac{kg}{m^3} \qquad \mu He := Y^{<3>} \cdot Pa \cdot sec \qquad kHe := Y^{<4>} \cdot \frac{watt}{m \cdot K} \qquad cpHe := Y^{<5>} \frac{joule}{kg \cdot K} \qquad HHe := Y^{<6>} \frac{joule}{kg}$$

$\rho He(T) := linterp(Temp, \rho He, T) \qquad \rho He(4 \cdot K) = 135.6 \, kg \cdot m^{-3}$

$\mu He(T) := linterp(Temp, \mu He, T) \qquad \mu He(65 \cdot K) = 7.5 \cdot 10^{-6} \cdot kg \cdot m^{-1} \cdot sec^{-1}$

$kHe(T) := linterp(Temp, kHe, T) \qquad kHe(65 \cdot K) = 0.056 \, m^{-1} \cdot K^{-1} \cdot watt$

$cpHe(T) := linterp(Temp, cpHe, T) \qquad cpHe(5 \cdot K) = 9163 \, kg^{-1} \cdot K^{-1} \cdot joule$

$HHe(T) := linterp(Temp, HHe, T) \qquad HHe(19.477 K) = 1.15 \cdot 10^{5} \cdot kg^{-1} \cdot joule$

C. Specific properties of water at 1 bar - Data from Chemical handbook

$Ywater := READPRN("water\_1bar.prn")$

$$cpwater := \left(Ywater^{<5>}\right) \frac{10^3 \cdot joule}{kg \cdot K} \qquad Temp := \left(Ywater^{<1>}\right) \cdot K$$

$cpwater(T) := linterp(Temp, cpwater, T) \qquad rhowater := \left(Ywater^{<2>}\right) \cdot 10^3 \frac{kg}{m^3} \qquad rhowater(T) := linterp(Temp, rhowater, T)$

$cpwater(300 \cdot K) = 0.998 \cdot \frac{cal}{10^{-3} \cdot kg \cdot K} \qquad viscwater := \left(Ywater^{<3>}\right) \cdot Pa \cdot sec \qquad rhowater(300 \cdot K) = 996.418 \frac{kg}{m^3}$

$T := 250 .. 390$

cp [Joule/kg/K]

4300

4179.42

273   Temperature [K]   320

Density [Kg/m^3]

1050

1000

950

900

300   350

Temperature [K]

<div style="display:flex">

| density | viscosity | conductivity | specific heat |
</div>

$$\rho H2O := Ywater^{<2>} \frac{10^3 \cdot kg}{m^3} \quad \mu H2O := Ywater^{<3>} \cdot Pa \cdot sec \qquad kH2O := Ywater^{<4>} \cdot \frac{watt}{m \cdot K} \qquad cpH2O := Ywater^{<5>} \cdot \frac{10^3 \cdot joule}{kg \cdot K}$$

$\rho H2O(T) := linterp(Temp, \rho H2O, T) \qquad \rho H2O(273 \cdot K) = 999.84 \, kg \cdot m^{-3}$

$\mu H2O(T) := linterp(Temp, \mu H2O, T) \qquad \mu H2O(273 \cdot K) = 0.002 \cdot Pa \cdot sec$

$kH2O(T) := linterp(Temp, kH2O, T) \qquad kH2O(273 \cdot K) = 0.561 \cdot \frac{watt}{m \cdot K}$

$cpH2O(T) := linterp(Temp, cpH2O, T) \qquad cpH2O(273 \cdot K) = 4217.6 \frac{joule}{kg \cdot K}$

D. Emissivity:

1. Aluminium (bluffed mechanicaly)

$$TAl := \begin{bmatrix} 4 \\ 80 \\ 300 \end{bmatrix} \cdot K \qquad EAl := \begin{bmatrix} 0.06 \\ 0.1 \\ 0.2 \end{bmatrix} \qquad eAl(t) := linterp(TAl, EAl, t)$$

2. Copper poli electrolitiquement

$$T := \begin{bmatrix} 4 \\ 77 \\ 300 \end{bmatrix} \cdot K \qquad Ecopper := \begin{bmatrix} 0.02 \\ 0.06 \\ 0.1 \end{bmatrix} \qquad ecopper(t) := linterp(T, Ecopper, t)$$

3. Stainless steel

$$ESS := \begin{bmatrix} 0.1 \\ 0.15 \\ 0.2 \end{bmatrix} \qquad eSS(t) := linterp(T, ESS, t)$$

Note : Tthe emissivity of Aluminum will be used for the characterisation of the CM, PS, PTS, and CTS instead of electrolitic polished copper which would give too optimistic results. Plus a factor 2 in the calculation was used to enhance the emissivity even further.

Emissivity general

$$E(esmall, elarge, Ssmall, Slarge) := \frac{1}{\left[\dfrac{1}{esmall} + \dfrac{Ssmall\left(\dfrac{1}{elarge} - 1\right)}{Slarge} \right]}$$

Definitions ==> $esmall := esmall(Tsmall)$

$elarge := elarge(Tlarge)$

$$E2(esmall, elarge, Ssmall, Slarge) := \frac{1}{\left[\dfrac{1}{esmall} + \left(\dfrac{1 - elarge}{elarge}\right) \cdot \left(\dfrac{Ssmall}{Slarge}\right) \right]}$$

Emissivity from ps to psts

$Tps = 273\,K$ $eps := 2\,eAl(Tps)$

$Tpsts = 78.3\,K$ $epsts := 2\,eAl(Tpsts)$ $Eps\_psts := E(eps, epsts, Sps, Spsts)$ $Eps\_psts = 0.115$

Emissivity from psts to ts

$eps = 0.375$

$epsts = 0.198$

$Tpsts = 78.5\,K$ $epsts := 2\,eAl(Tpsts)$

$TcryostatTS = 79.5\,K$ $ets := 2\,eAl(TcryostatTS)$ $Epsts\_ts := E(epsts, ets, Spsts, Stsbellows)$ $Epsts\_ts = 0.169$

Emissivity from bs to cm

$Tbs = 80.3\,K$ $ebs := 2\,eAl(Tbs)$ $ebs = 0.2$

$Tcm = 19\,K$ $ecm := 2\,eAl(Tcm)$ $ecm = 0.136$

Emissivity from ts to cm

$Ebs\_cm := E(ebs, ecm, Sbs, Scm)$ $Ebs\_cm = 0.115$

$Tcm = 19\,K$ $ecm := 2\,eAl(Tcm)$

$TcryostatTS = 79.5\,K$ $ets := 2\,eAl(TcryostatTS)$ $Ets\_cm := E(ecm, ets, Scm, Surf\_cryostatTS)$ $Ets\_cm = 0.126$

$Tend = 99.5\,K$ $ets\_end := 2\,eAl(Tend)$ $Ets\_cm\_end := E(ecm, ets, Scm, Sendcap)$ $Ets\_cm\_end = 0.095$

Emissivity from ps to bs

$Tbs = 80.3 \cdot K$ $ebs := 2 \, eAl(Tbs)$

$Tps = 273 \cdot K$ $eps := 2 \, eAl(Tps)$ $eps = 0.375$

$Eps\_bs := E(ebs, ecm, Sbs, Scm)$ $Eps\_bs = 0.115$

Cryostat Thermal shield

$T := \begin{bmatrix} 4 \\ 80 \\ 300 \end{bmatrix} \cdot K$ $ESS := \begin{bmatrix} 0.1 \\ 0.15 \\ 0.2 \end{bmatrix}$ $eSS(t) := linterp(T, ESS, t)$

$TMyl := \begin{bmatrix} 4 \\ 80 \\ 300 \end{bmatrix} \cdot K$ $EMyl := \begin{bmatrix} 0.04 \\ 0.08 \\ 0.15 \end{bmatrix}$ $eMyl(t) := linterp(TMyl, EMyl, t)$

$$Evv\_tsMyl(Tc, Tf) := \cfrac{1}{\left[\cfrac{1}{eMyl(Tf)} + \cfrac{Surf\_cryostatVV \cdot \left(\cfrac{1}{eSS(Tc)} - 1 \right)}{Surf\_cryostatTS} \right]}$$

$Evv\_tsMyl := Evv\_tsMyl(Tvv, TcryostatTS)$ $Evv\_tsMyl = 0.058$

E. Conduction in residual gas though MLI

Data [CERN data]:
$TcryostatTS = 79.5 \cdot K$

There are $N10 := 10$ layers of MLI on the RS

There are $N30 := 30$ layers of MLI on the TS

$Tvv = 300 \cdot K$

$$Qvv\_ts(a, b, A) := \left[\frac{a}{N30} \cdot \left(\frac{Tvv^2 - TcryostatTS^2}{2} \right) + \frac{b}{N30} \cdot \left(Tvv^4 - TcryostatTS^4 \right) \right] \cdot A$$

Values of a and b for different pressures:

1E-6 bar $a6 := 1.4 \cdot 10^{-4} \cdot \frac{watt}{m^2 \cdot K^2}$ $b6 := 3.74 \cdot 10^{-9} \cdot \frac{watt}{m^2 \cdot K^4}$

1E-3 bar $a3 := 6.544 \cdot 10^{-3} \cdot \frac{watt}{m^2 \cdot K^2}$ $b3 := -2.166 \cdot 10^{-8} \cdot \frac{watt}{m^2 \cdot K^4}$

1E-2 bar $a2 := 0.05 \frac{watt}{m^2 \cdot K^2}$ $b2 := -2.212 \cdot 10^{-7} \cdot \frac{watt}{m^2 \cdot K^4}$

3. CALCULATIONS

3.1 TO cold mass - Cold Helium circuit

A. Radiation   Recall => $Ebs\_cm = 0.115$ $Ltsbellow = 28 \cdot in$ $Sbs = 0.182 m^2$ $Tcm = 19 K$ $Tend = 99.5 K$

$Ets\_cm = 0.126$ $Abs\_cm = 7.114 \cdot 10^{-4} \cdot m^2$ $Scm = 0.316 m^2$ $TcryostatTS = 79.9 K$ $Tbs = 80.9 K$

$eSS(Twater) = 0.197$

$Qts\_cm := Ets\_cm \cdot \sigma \cdot (TcryostatTS^4 - Tcm^4) \cdot Scm$ $\boxed{Qts\_cm = 0.09 \cdot watt}$ $\boxed{\dfrac{Qts\_cm}{(TcryostatTS^4 - Tcm^4)} = 2.268 \cdot 10^{-9} \cdot K^{-4} \cdot watt}$

$Qbs\_cm := Ebs\_cm \cdot \sigma \cdot (Tbs^4 - Tcm^4) \cdot Sbs$ $\boxed{Qbs\_cm = 0.05 \cdot watt}$ $\boxed{\dfrac{Qbs\_cm}{(Tbs^4 - Tcm^4)} = 1.194 \cdot 10^{-9} \cdot K^{-4} \cdot watt}$

$Qend\_cm := Ets\_cm\_end \cdot \sigma \cdot (Tend^4 - Tcm^4) \cdot Scm$ $\boxed{Qend\_cm = 0.167 \cdot watt}$ $\boxed{\dfrac{Qend\_cm}{(Tend^4 - Tcm^4)} = 1.708 \cdot 10^{-9} \cdot K^{-4} \cdot watt}$

For optimization purpose, water circuit influence was added: assumption : 1/3.5 of the CM sees the tube

$Qwaterpipe\_cm := eSS(Twater) \cdot \sigma \cdot \left[(Twater)^4 - Tcm^4\right] \dfrac{Scm}{3.5}$ $\boxed{Qwaterpipe\_cm = 6.643 \cdot watt}$ $\boxed{\dfrac{Qwaterpipe\_cm}{\left[(Twater)^4 - Tcm^4\right]} = 1.007 \cdot 10^{-9} \cdot K^{-4} \cdot watt}$

$Qwaterpipe\_emis := eSS(Twater) \cdot \sigma \cdot \left[(Twater)^4\right] \cdot Scm$ $\dfrac{Qwaterpipe\_emis}{3.5} = 6.644 \cdot watt$

B. Conduction   Recall => $Abs\_cm = 7.114 \cdot 10^{-4} \cdot m^2$ $Lbs\_cm = 0.016 m$ $Twater = 285 K$

$Ats\_bellows = 3.584 \cdot 10^{-5} \cdot m^2$ $Ltsbellow = 0.711 m$ $Tvv = 300 K$

$Qcon\_bs\_cm := \left(\displaystyle\int_{Tcm}^{Tbs} kG10(T)dT \cdot \dfrac{Abs\_cm}{Lbs\_cm}\right)$ $\boxed{Qcon\_bs\_cm = 0.797 \cdot watt}$ $\boxed{\dfrac{Qcon\_bs\_cm}{(Tbs - Tcm)} = 0.013 K^{-1} \cdot watt}$

$Qcon\_ts\_cm := \left(\displaystyle\int_{Tcm}^{TcryostatTS} kSS(T)dT \cdot \dfrac{Ats\_bellows}{Ltsbellow}\right)$ $\boxed{Qcon\_ts\_cm = 0.017 \cdot watt}$ $\boxed{\dfrac{Qcon\_ts\_cm}{(TcryostatTS - Tcm)} = 2.756 \cdot 10^{-4} \cdot K^{-1} \cdot watt}$

C. Total static heat loads

With no water lines influence but with end cap influence

$Qcm := Qend\_cm + Qts\_cm + Qbs\_cm + Qcon\_bs\_cm + Qcon\_ts\_cm$

With water lines influence and end cap $\boxed{Qcm = 1.121 \cdot watt}$

$Qcm := Qend\_cm + Qts\_cm + Qbs\_cm + Qcon\_bs\_cm + Qcon\_ts\_cm + Qwaterpipe\_cm$

$\boxed{Qcm = 7.765 \cdot watt}$

3.2 TO the Beam screen - Warm Helium circuit

Recall => $Ats\_bs = 6 \cdot 10^{-4} \cdot m^2$ $Lpstsbellows = 0.61 \cdot m$ $Tbs = 80.5 \cdot K$ $Tps = 273 \cdot K$

   $Ats\_bellows = 3.584 \cdot 10^{-5} \cdot m^2$ $Lts\_bs = 0.392 \cdot m$ $TcryostatTS = 79.5 \cdot K$

$RPTS := 350 in$ RPTS is by design 350 in

A. Radiation   Assumption of the surface seing the ps nose : Sbs/2

$Qradps\_bs := Eps\_bs \cdot \sigma \cdot (Tps^4 - Tbs^4) \dfrac{Sbs}{2}$ $Qradps\_bs = 3.292 \cdot watt$ $\dfrac{Qradps\_bs}{(Tps^4 - Tbs^4)} = 5.971 \cdot 10^{-10} \cdot K^{-4} \cdot watt$

B. Conduction

$Qcon\_ps\_bs := \dfrac{1}{2} \cdot \left(\displaystyle\int_{Tbs}^{Tps} kG10(T)\,dT \dfrac{Aps\_psts}{Lbs\_ps} \right)$ $Qcon\_ps\_bs = 1.7 \cdot watt$ $\dfrac{Qcon\_ps\_bs}{Tps - Tpsts} = 0.009 K^{-1} \cdot watt$

C. Total static heat loads

$Qbs := Qradps\_bs + Qcon\_ps\_bs$ $Qbs = 4.991 \cdot watt$

3.3 TO photon stop thermal shield: tsps Warm Helium circuit

A. Radiation   Recall => $Tpsts = 78.5 \cdot K$ $Spsts = 0.037 \, m^2$ $Tbs = 80.5 \cdot K$ $Aps\_psts = 9.501 \cdot 10^{-5} \cdot m^2$

$Tcm = 19 \cdot K$ $Tps = 273 \cdot K$ $Tps = 273 \cdot K$ $Apsts\_bellows = 3.314 \cdot 10^{-5} \cdot m^2$

$Qps\_psts := Eps\_psts \cdot \sigma \cdot (Tps^4 - Tpsts^4) \cdot Sps$ $Qps\_psts = 1.973 \cdot watt$ $\dfrac{Qps\_psts}{(Tps^4 - Tpsts^4)} = 3.576 \cdot 10^{-10} \cdot K^{-4} \cdot watt$

B. Conduction

$Qcon\_psts\_ps := \dfrac{1}{2} \cdot \left(\displaystyle\int_{Tpsts}^{Tps} kG10(T)\,dT \dfrac{Aps\_psts}{Lbs\_ps} \right)$ $Qcon\_psts\_ps = 1.711 \cdot watt$ $\dfrac{Qcon\_psts\_ps}{Tps - Tpsts} = 0.009 K^{-1} \cdot watt$

$Qcon\_rt\_tsps := \displaystyle\int_{Tpsts}^{Tvv} kSS(T)\,dT \dfrac{Apsts\_bellows}{Lpstsbellows}$ $Qcon\_rt\_tsps = 0.148 \cdot watt$ $\dfrac{Qcon\_rt\_tsps}{Tvv - Tpsts} = 6.693 \cdot 10^{-4} \cdot K^{-1} \cdot watt$

C. Total static heat loads

$Qtsps := Qps\_psts + Qcon\_psts\_ps + Qcon\_rt\_tsps$ $Qtsps = 3.832 \cdot watt$

3.4 To Cryostat Thermal shield - Warm Helium circuit

A. Radiation

With no MLI

$W6vv\_tsMyl := Evv\_tsMyl \cdot \sigma \cdot Surf\_cryostatTS \cdot \left(Tvv^4 - TcryostatTS^4\right)$ $W6vv\_tsMyl = 61.866 \, watt$

With MLI

$QcryostatTS := Qvv\_ts(a6, b6, Surf\_cryostatTS)$ $QcryostatTS = 2.813 \, watt$ $\dfrac{QcryostatTS}{\left(Tvv^4 - TcryostatTS^4\right)} = 3.49 \, 10^{-10} \cdot K^{-4} \cdot watt$

B. Conduction

$Qcon\_vv\_cts := \left(\displaystyle\int_{TcryostatTS}^{Tvv} kG10(T)\,dT \cdot \dfrac{Aspider}{Lspider}\right)$ $Qcon\_vv\_cts = 1.527 \, watt$ $\dfrac{Qcon\_vv\_cts}{Tvv - TcryostatTS} = 0.007 \, K^{-1} \cdot watt$

C. Total static heat loads

$Qts := Qcon\_vv\_cts + QcryostatTS$ $Qts = 4.34 \, watt$

4 - PARASITIC HEAT LOAD ESTIMATIONS

4.1- From heater YCM to sensors TCou

Assumption: Heater size = 1in* 5 in: see Omega catalogue, model: KHLV-105-10

$Theater := 300\,K$ Assumption heater temperature = 300K

$Qheater\_cm := 1 \cdot \sigma \cdot \left[(Theater)^4 - Tcm^4 \right] \cdot (1 \cdot in \cdot 5 \cdot in)$ $\boxed{Qheater\_cm = 1.481 \cdot watt}$

4.2- From heater water supply line to the system

Assumptions : Water line size = 0.5 in dia* 50 cm long * 2 tubes

$diawaterpipe = 0.013\,m$

$Lwater = 0.5\,m$ $Scm = 0.316\,m^2$

$Twaterline := 271 \cdot K$

$Qwaterline\_cm := 1 \cdot \sigma \cdot \left[(Twaterline)^4 \right] \cdot Swaterpipe$ $\boxed{Qwaterline\_cm = 12.195 \cdot watt}$

4.3- Calculation of the CX sensors temperature raise

$Ratio := \left[\dfrac{(60 \cdot in \cdot 3.14 \cdot (20 \cdot in))}{\left(mm^2 \cdot 3.2 \cdot 1.9 + 1\,mm \cdot 3.2 \cdot mm \cdot 2 + 1\,mm \cdot 1.9 \cdot mm \cdot 2 \right)} \right]^{-1}$ $Ratio = 6.697 \cdot 10^{-6}$

$cp := 20 \dfrac{joule}{kg \cdot K}$: Specific heat ceramic

$M := 40 \cdot 10^{-6} \cdot kg$: Mass of the temperature sensor

$k := 0.146 \dfrac{watt}{K \cdot m}$: Conductivity of the temperature sensor

$rho := 2770 \dfrac{kg}{m^3}$: Density of the temperature sensor

$diff := \dfrac{k}{cp \cdot rho}$: Diffution equation $diff = 2.635 \cdot 10^{-6} \cdot \dfrac{m^2}{sec}$

$DT := \dfrac{Qwaterline\_cm \cdot Ratio \cdot \left(3.2 \cdot 10^{-3} \cdot m \right)^2}{M \cdot cp \cdot diff}$: Temperature raise expected $\boxed{DT = 0.397 \cdot K}$

Conclusion :   TCX4 must be increased of 0.4 K for Twater=270 K
                      TCX4 must be increased of 1.4 K for Twater =370 K
                      Qwater line is 12 W for Twater=270 W
                      Qwater line is 42.4 W for Twater=370 W

5. FLOW CALCULATIONS

5.1- Powers

efficiency $:= 0.3$

$$carnot(T) := \frac{1}{\left(\frac{T}{300 \cdot K - T}\right) \cdot efficiency}$$ carnot$(5 \cdot K) = 196.667$

Qps4K $:= 50 \cdot watt$: Electrical heat at 4 K

Qps $:=$ Qps4K   Qps $= 50 \cdot watt$

Recall =>
Tpsout $= 276 \cdot K$	Qps $= 50 \cdot watt$	Qtsps $= 3.832 \cdot watt$	Qps $= 50 \cdot watt$
Tpsin $= 270 \cdot K$	Qbs $= 4.991 \cdot watt$	QcryostatTS $= 2.813 \cdot watt$	Qcm $= 7.765 \cdot watt$

5.2 - Water loop

$$mdotwater := \frac{Qps + 4 \cdot 50 \cdot watt}{cpH2O(Tps) \cdot (Tpsout - Tpsin)}$$

mdotwater $= 0.01 \cdot kg \cdot sec^{-1}$

$$\frac{mdotwater}{\rho H2O(273 \cdot K)} = 9.397 \cdot \frac{gal}{hr}$$

5.3 - Warm helium loop

QN2 $:=$ Qtsps $+$ QcryostatTS $+$ Qbs $+ 3 \cdot 50 \cdot watt$ QN2 $= 161.636 \cdot watt$

$$mdotN2 := \frac{QN2}{cpHe(80 \cdot K) \cdot (Tbsout - Tpstsin)}$$

mdotN2 $= 0.01 \cdot kg \cdot sec^{-1}$

5.5 - LHe loop   Qcm $= 7.765 \cdot watt$

QHe $:=$ Qcm $+ ˜0 \cdot watt$

$$mdotHe := \frac{QHe}{cpHe(5 \cdot K) \cdot (1 \cdot K)}$$

mdotHe $= 0.006 \cdot kg \cdot sec^{-1}$

APPENDIX H – SUMMARY OF EXPERIMENTAL DATA (RAW)

The following tables contain the residual heat load data obtained with the static method for all major sub-systems (cold mass CM, photon stop thermal shield PTS, beam screen BS and cryostat thermal shield) together with the temperatures from which the heat loads were calculated.

	TCM	TPTS	TCTS	TBS	Tnose	TCCMIN	TCCMOU	QCM_stat TCM=15 K	QCM_stat TCM=24 K	g/s
A	15.96	50.685	47.29	48.95	271.00	0.00	0.00	7.76	-	0.89628
B	14.64	80.98	77.00	76.11	271.00	13.39	15.27	10.71	-	0.97695
C*	12.25	51.345	45.85	46.042	271.00	0.00	0.00	-	-	
D	23.59	48.41	45.15	44.97	271.00	20.66	22.39	-	2.54	0.29622
E	22.29	48.87	44.97	46.535	360.00	21.26	23.41	-	2.99	0.30711
F	14.37	75.315	72.52	71.075	271.00	13.26	15.08	9.67	-	1.05975
G	15.20	77.025	72.01	71.735	376.00	14.20	15.82	8.94	-	1.02583
H	24.54	48.415	44.88	44.8	271.00	23.94	25.10	-	1.78	0.32325
I	25.13	49.82	45.81	45.7	377.00	23.98	26.28	-	3.60	0.299
J	24.00	45.435	43.46	43.365	83.00	23.72	24.55	-	1.13	0.30167
K	13.08	45.68	43.53	44.145	85.00	12.48	13.34	1.15	-	1.0055

	TCM	TPTS	TCTS	TBS	Tnose	TPBSIN	TPBSOU	QBS_stat	g/s
A	15.96	50.685	47.29	48.95	271.00	49.1	48.8	-26.42	0.9535
B	14.64	80.98	77.00	76.11	271.00	78.82	73.4	-28.13	1.00767
C*	12.25	51.345	45.85	46.042	271.00	48.383	43.7		0.99933
D	23.59	48.41	45.15	44.97	271.00	47.74	42.2	-30.36	1.0335
E	22.29	48.87	44.97	46.535	360.00	47.9	45.17	-14.05	1.00967
F	14.37	75.315	72.52	71.075	271.00	73.74	68.41	-139.25	5.02075
G	15.20	77.025	72.01	71.735	376.00	74.19	69.28	-128.20	4.99667
H	24.54	48.415	44.88	44.8	271.00	47.53	42.07	-28.56	1.007
I	25.13	49.82	45.81	45.7	377.00	48.16	43.24	-26.02	1.017
J	24.00	45.435	43.46	43.365	83.00	46.21	40.52	-29.50	0.998
K	13.08	45.68	43.53	44.145	85.00	47.08	41.21	-31.84	1.062

	TCM	TPTS	TCTS	TBS	Tnose	TPPTSIN	TPPTSOU	QPTS_stat	g/s
A	15.96	50.685	47.29	48.95	271.00	49.35	52.02	50.69	0.9535
B	14.64	80.98	77.00	76.11	271.00	79.38	82.58	16.64	1.00767
C*	12.25	51.345	45.85	46.042	271.00	49.89	52.8	-	0.99933
D	23.59	48.41	45.15	44.97	271.00	46.96	49.86	15.28	1.0335
E	22.29	48.87	44.97	46.535	360.00	47.2	50.54	19.76	1.00967
F	14.37	75.315	72.52	71.075	271.00	73.84	76.79	77.22	5.02075
G	15.20	77.025	72.01	71.735	376.00	75.26	78.79	91.89	4.99667
H	24.54	48.415	44.88	44.8	271.00	46.99	49.84	14.92	1.007
I	25.13	49.82	45.81	45.7	377.00	48	51.64	19.25	1.017
J	24.00	45.435	43.46	43.365	83.00	44.53	46.34	9.37	0.998
K	13.08	45.68	43.53	44.145	85.00	44.86	46.5	9.06	1.062

	TCM	TPTS	TCTS	TBS	Tnose	TPTSIN	TPTSOU	QCTS_stat	flow
A	15.96	50.685	47.29	48.95	271.00	45.54	49.03	17.3041	0.9535
B	14.64	80.98	77.00	76.11	271.00	74.68	78.49	19.9639	1.00767
C*	12.25	51.345	45.85	46.042	271.00	44.2	47.5	17.1486	0.99933
D	23.59	48.41	45.15	44.97	271.00	43.5667	46.7333	17.0183	1.0335
E	22.29	48.87	44.97	46.535	360.00	43.6	46.3333	14.3507	1.00967
F	14.37	75.315	72.52	71.075	271.00	71.2	73.8375	68.8596	5.02075
G	15.20	77.025	72.01	71.735	376.00	70.9	73.125	57.8114	4.99667
H	24.54	48.415	44.88	44.8	271.00	43.4	46.35	15.4474	1.007
I	25.13	49.82	45.81	45.7	377.00	44.375	47.25	15.2042	1.017
J	24.00	45.435	43.46	43.365	83.00	42.05	44.875	14.6606	0.998
K	13.08	45.68	43.53	44.145	85.00	42	45.05	16.8433	1.062

The following table contains the residual heat loads for all sub-systems measured with method 2. The table does not contain the temperature data.

	TCM	TPTS	TCTS	TBS	Tnose	QCM2	QPTS2	QBS2	QCTS2
A	15.96	50.685	47.29	48.95	271.00	-	-	-	-
B	14.64	80.98	77.00	76.11	271.00	8.76	14.7	-28.08	12.97
C*	12.25	51.345	45.85	46.042	271.00	22.81	-	-	-
D	23.59	48.41	45.15	44.97	271.00	4.67	13.9	-31.91	-
E	22.29	48.87	44.97	46.535	360.00	6.16	17.7	-29.05	-
F	14.37	75.315	72.52	71.075	271.00	8.45	79.89	-141.19	-
G	15.20	77.025	72.01	71.735	376.00	7.74	94.2	-129.8	-
H	24.54	48.415	44.88	44.8	271.00	-9.28	-	-	-
I	25.13	49.82	45.81	45.7	377.00	3.16	-	-	-
J	24.00	45.435	43.46	43.365	83.00	0.02	7.71	-30.71	-
K	13.08	45.68	43.53	44.145	85.00	-0.69	-	-	-

APPENDIX I – CALIBRATION OF T-SENSORS
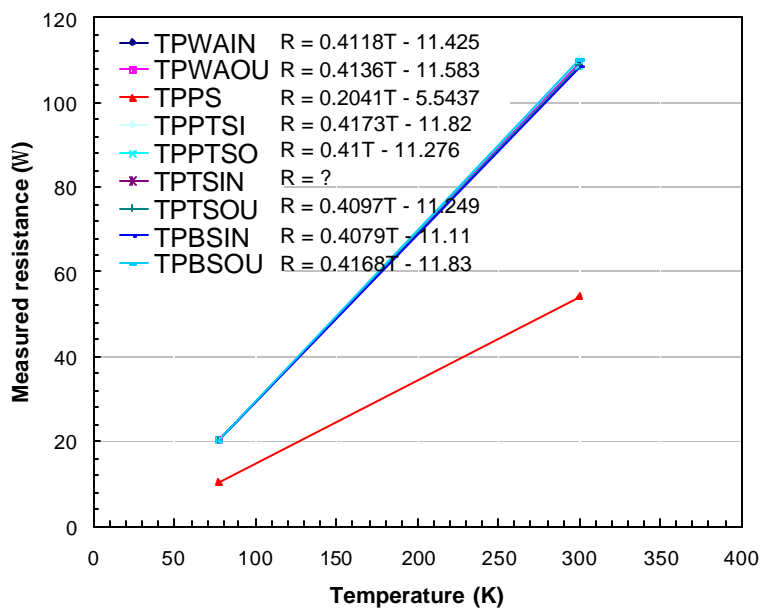
Figure 32: Platinum sensor calibration at room temperature and in LN bath. No measurement data available for sensor TPTSIN. See Table 1 for naming convention.

TCCMIN

Data: Data1_B
Model: ExpDec3
Equation: y = A1*exp(-x/t1) + A2*exp(-x/t2) + A3*exp(-x/t3) + y0
Weighting:
y   No weighting

Chi^2/DoF   = 317.57812
R^2   = 0.99985

y0	86.16316	±4.06423
A1	63677.07173	±7412.41639
t1	1.06217	±0.0493
A2	5932.39878	±352.25032
t2	4.76506	±0.19653
A3	1091.7318	±39.58276
t3	37.33618	±1.42685

TCCM3

Data: TCCM3data_B
Model: ExpDec3
Equation: y = A1*exp(-x/t1) + A2*exp(-x/t2) + A3*exp(-x/t3) + y0
Weighting:
y   No weighting

Chi^2/DoF   = 394.232
R^2   = 0.99982

y0	88.56542	±4.432
A1	6657.96072	±434.16526
t1	4.44491	±0.19203
A2	77238.50289	±11598.85043
t2	0.99203	±0.05429
A3	1162.00018	±43.1655
t3	35.59091	±1.39989

TCCMOU

Data: TCCMOUdata_B
Model: ExpDec3
Equation: y = A1*exp(-x/t1) + A2*exp(-x/t2) + A3*exp(-x/t3) + y0
Weighting:
y   No weighting

Chi^2/DoF   = 477.25671
R^2   = 0.99983

y0   90.22997   ±4.78671
A1   7765.20833   ±519.82488
t1   4.27675   ±0.18455
A2   94848.51175   ±14620.03249
t2   0.96809   ±0.05302
A3   1276.8931   ±48.95132
t3   33.86214   ±1.34873

TCCMM1

Data: TCCMM1data_B
Model: ExpDec3
Equation: y = A1*exp(-x/t1) + A2*exp(-x/t2) + A3*exp(-x/t3) + y0
Weighting:
y   No weighting

Chi^2/DoF   = 898.47018
R^2   = 0.9996

y0   98.61059   ±6.17282
A1   1430.7948   ±58.99971
t1   28.81537   ±1.29554
A2   302676.7009   ±170343.33435
t2   0.66221   ±0.08063
A3   10819.34765   ±953.11659
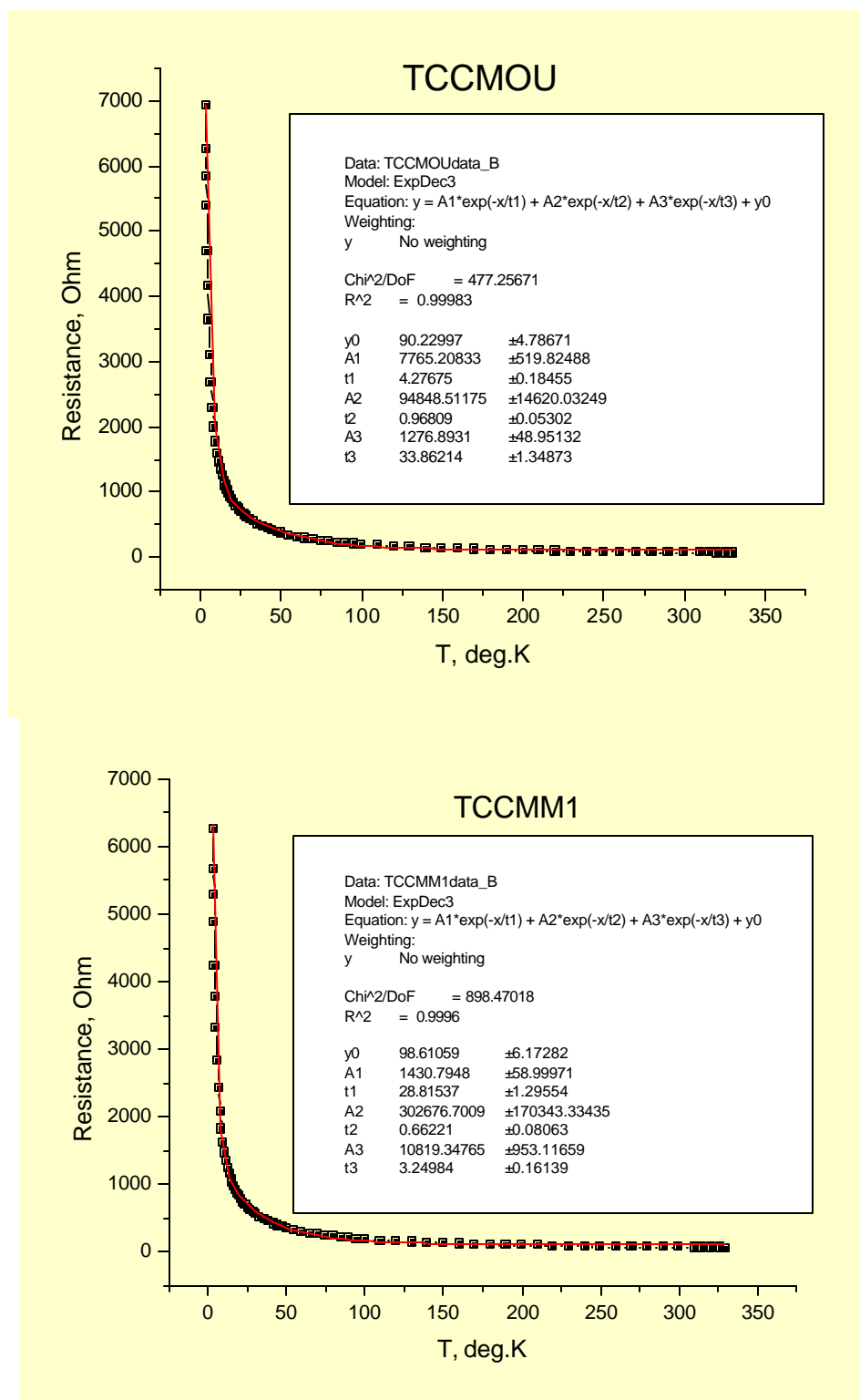t3   3.24984   ±0.16139

Figure 33: Cernox sensor calibrations as provided by LakeShore™. See Table 1 for naming convention.